DIFFUSION IN TWO DIMENSIONAL MAPPINGS

by

A. J. Lichtenberg and M. A. Lieberman

DIFFUSION IN TWO DIMENSIONAL
MAPPINGS

by

A. J. Lichtenberg and M. A. Lieberman

ELECTRONICS RESEARCH LABORATORY

College of Engineering
University of California, Berkeley
94720

DIFFUSION IN TWO DIMENSIONAL
MAPPINGS

by

A. J. Lichtenberg and M. A. Lieberman

ELECTRONICS RESEARCH LABORATORY

Diffusion in Two Dimensional Mappings

A.J. Lichtenberg and M.A. Lieberman

Department of Electrical Engineering and Computer Sciences

and the Electronics Research Laboratory

University of California, Berkeley CA 94720

ABSTRACT

Two dimensional mappings are used to model both Hamiltonian and dissipative systems in two degrees of freedom. Numerical iterations of these mappings are then easily performed to reveal the phase space structure, transient and invariant phase space density distributions, and the rate of transport of phase points in "time" (mapping periods). Mappings are chosen for their generic quality, their convenience in analysis, or their close correspondence to physical systems. For Hamiltonian systems (Part I), the self-similar structure of the phase space at all scales leads to long-time correlations of trajectories that decay more slowly than exponentially. The result of these correlations is to modify the quasilinear diffusion rate, which can be calculated to an arbitrary degree of accuracy for mappings which are on a torus (periodic in both action and angle). For generic mappings, in which only the angle is periodic, approximate local diffusion coefficients (averaged over phase) can be obtained and used in a Fokker-Planck equation to determine phase space transport in action. For mappings on a torus, some values of parameters give rise to accelerator modes, which lead to streaming particles for which the diffusion rate may be infinite. For generic mappings which are periodic only in angle, these accelerator modes enhance diffusion but do not lead to singularities. The diffusion coefficient is also obtained for systems in the adiabatic limit in which the small parameter is the ratio of the unperturbed frequencies. For dissipative systems (Part II), transport and phase space distributions are considered both for parameter ranges in which regular attractors exist and parameter ranges having a chaotic (strange) attractor. Particular attention is given to dissipative mappings in which the dissipation is a perturbation from an area preserving (Hamiltonian) mapping. For small dissipation, the rate of decay of the phase space density,

by absorption into regular attractors (sinks) is shown to increase with the dissipation parameter δ in an easily calculable manner. With continued increase in δ, more subtle phenomena appear which lead to a maximum rate of density decay at some $\delta = \delta_s$ and then to a vanishing phase averaged decay rate at some $\delta = \delta_{cr}$, beyond which a strange attractor exists. A method of calculating the invariant distribution on the attractor to arbitrary accuracy is described.

Introduction

The study of non-linear dynamical systems has revealed many examples of chaotic behavior. The simplest systems in which such behavior is observed are two degree-of-freedom Hamiltonian systems and their dissipative counterparts. Two dimensional area preserving mappings, which have a Hamiltonian structure, may be used to model the Hamiltonian systems. These can be smoothly transformed into dissipative mappings by variation of a parameter.

The phase space structure in two-dimensional near-integrable measure-preserving maps is intricate. There is persistent regular motion on perturbed KAM orbits and on KAM island orbits surrounding stable fixed points of the map. Regions of persistent chaotic motion are densely interwoven with these regular regions. The measures of the regular and the chaotic regions can vary widely, both within the phase plane and as a function of the system parameters.

New phenomena appear for dissipative systems. Since the (two-dimensional) area of the Poincaré surface of section contracts (by the Jacobian factor J of the map) after each iteration, the motion ultimately lies on a set of lower dimensionality called an attractor. For large dissipation ($J \ll 1$), one or more chaotic (strange) attractors having fractional dimensionality can exist. It is natural to ask whether persistent chaos continuously exists when a Hamiltonian system is smoothly transformed into a dissipative system. The numerical evidence suggests that this does not occur. Instead, an intervening regime of weak dissipation ($1-J \ll 1$) appears for which all persistent chaotic motion is destroyed. Although the motion may be transiently chaotic over hundreds of thousands of iterations, ultimately the trajectory is attracted to a periodic orbit.

In addition to describing the detailed motion of chaotic orbits it is often useful to predict the statistical properties of families of orbits. In many problems, the evolution of only one of the two phase space variables, the action (or the energy), is of interest. If we assume that the phase variable is randomized much more rapidly than the action, then it may be possible to describe the dynamics using a Fokker-Planck equation for the evolution of the distribution of actions $f(u,n)$, where u is the action and, for a mapping, n is the "time", in units of the mapping period.

We restrict our attention in this review to two degrees of freedom without external noise. Considerable work has been done on extensions to include external stochasticity and to obtain results with three degrees of freedom. These topics are reviewed and references to the literature given in ref [1]. For more than three degrees of freedom it was early realized that the phase space tends toward ergodicity [2], but few detailed calculations have been made [1, Sec. 6.5].

In Part I we consider Hamiltonian systems. In Section A we introduce the area preserving mappings that have proven convenient for analyzing such systems, either because of their genericity or because of their simplicity. In Section B the structure of the phase space is discussed. The methods for determining the coefficients of the Fokker-Planck equation, including phase correlations, are considered in Section C. This is followed in Section D by calculations of the distribution function and transport properties using the Fokker-Planck formalism.

In Part II dissipative systems are considered, with the emphasis being on continuous transformation away from the area preserving mappings. In Section A the phenomenon of transient chaos is treated, including both the calculation of the transient distribution, using a Fokker-Planck equation, and the calculation of the absorption rate into the stable attracting fixed points. In Section B the transition from transient chaos to a chaotic attractor is considered. Finally, in Section C, the calculation of steady-state distributions on chaotic attractors is described.

I. Hamiltonian Systems

A. *Mappings as Dynamical Systems*

We consider either autonomous Hamiltonian systems in two degrees of freedom, $H = H(z)$, where $z = (p_1, p_2, q_1, q_2)$, or nonautonomous Hamiltonian systems in one degree of freedom, $H' = H'(p_1, q_1, t)$. The latter systems can be made autonomous in two degrees of freedom by introducing a new Hamiltonian [1, Sec. 2.1]

$$H(z) = H'(p_1, q_1, q_2) + p_2 \tag{1}$$

defined on the extended phase space $(p_1, p_2 = -H', q_1, q_2 = t)$.

To define an area-preserving map for this system, we introduce a surface of section Σ_R in the phase space (see Fig. 1.3a), as follows: Since the motion of the phase point $z(t)$ in the four dimensional phase space lies on a constant energy surface $H(z) = $ const, (see Fig. 1.3b) we can solve for one of the canonical variables, say p_2, in terms of the others:

$$p_2 = p_2(\mathbf{x}, q_2) \tag{2}$$

where $\mathbf{x} = (p_1, q_1)$. We define a particular Σ_R by the condition $q_2 = $ const. As the phase point z evolves with time, it repeatedly pierces (in the same direction) Σ_R. As shown in Fig. 1.3a, the successive intersections n, $n+1$, $n+2$, etc. of the trajectory with Σ_R generate a two-dimensional map

$$\mathbf{x}_{n+1} = T(\mathbf{x}_n) . \tag{3}$$

For this particular choice of Σ_R, the map is area-preserving; i.e., the Jacobian $J = \partial \mathbf{x}_{n+1} / \partial \mathbf{x}_n$ is unity [1, Sec. 3.1]. There are two such surfaces of section of immediate physical interest: (p_1, q_1) for $q_2 = $ const and (p_2, q_2) for $q_1 = $ const. If the phase points are conserved in the motion (no sources or sinks), an immediate consequence of area-preservation is that the equilibrium invariant distribution within the chaotic region of the surface of section is uniform, independent of $\mathbf{x}$.

As an illustration of these concepts consider the problem of a ball bouncing in one dimensional motion along x between a fixed and an oscillating wall, which we shall call the Fermi acceleration configuration. We can write the difference equations for the motion, using a fixed surface of section $x = $ const. Defining $u_n = v_n / 2\omega a$ to be the normalized velocity, θ_n to be the phase of the moving wall at the nth collision of the ball with the fixed surface $x = 0$ about which the wall oscillates, and with a wall motion $x = aF_l(\psi)$, where F_l is an even periodic function of the phase $\psi = \omega t$, with period 2π and with $F_{lmax} = -F_{lmin} = 1$, we have, in implicit form, the equations of motion [1, Sec. 3.4]

$$u_{n+1} = u_n + F(\psi_c) , \tag{4a}$$

$$\theta_{n+1} = \psi_c + \frac{[2\pi M - \frac{1}{2} F_I(\psi_c)]}{u_{n+1}} \, , \tag{4b}$$

$$\psi_c = \theta_n - \frac{1}{2} \frac{F_I(\psi_c)}{u_n} \, . \tag{4c}$$

Here ψ_c is the phase at the next collision with the moving wall, after the nth collision with the fixed surface $x = 0$, $M = l/2\pi a$, with l the distance between the walls, and $F = dF_I/d\psi$ is the velocity impulse given the ball. In this form it is easy to see that measuring the distance from the fixed wall as x, conjugate to v, then the phase θ is a time-like variable conjugate to the energy $E = u^2$. That is, in the extended phase space $(v, x, -E, t)$, the choice of a surface of section $x = 0$ gives an area-preserving mapping for the remaining pair $(-E, \theta)$. This can be confirmed by direct computation of the Jacobian yielding

$$J \equiv \frac{\partial(E_{n+1}, \theta_{n+1})}{\partial(E_n, \theta_n)} = 1 \, . \tag{5}$$

Thus the normalized energy E has a uniform invariant distribution.

Because of its implicit form (4) is not convenient for numerical or analytical study. A much simpler form can be constructed if the oscillating wall imparts momentum to the ball, according to the wall velocity, without the wall changing its position in space. The problem defined in this manner has many of the features of the more physical problem and can be analytically treated with various wall-forcing functions. In this simplified form the mapping is [3; 1, Sec. 3.4]

$$u_{n+1} = u_n + F(\psi_n) \tag{6a}$$

$$\psi_{n+1} = \psi_n + \frac{2\pi M}{u_{n+1}}. \tag{6b}$$

A fundamental difference between (4) and (6), however, is that the canonical variables are different, leading to different variables in which the invariant distribution is a constant. For the simplified problem (6), a proper canonical set of variables are the ball velocity and phase just before the nth impact with the moving wall. The normalized velocity u then has a constant invariant distribution, as will be seen in Sec. IB.

Keeping these considerations in mind, a very useful map for investigating dynamics of physical systems is the simplified Fermi map with a sinusoidal forcing function

$$u_{n+1} = u_n + \sin \psi_n$$
$$\psi_{n+1} = \psi_n + \frac{2\pi M}{u_{n+1}} \pmod{2\pi} . \tag{7}$$

The mapping in (7) serves as an approximation (with suitably defined variables) to many physical systems in which the transit time between kicks is inversely proportional to a velocity, such as cyclotron resonance heating in a magnetic mirror [4], electron heating in sheaths of an r.f. capacitive discharge [5] and the free motion of nucleons in a nucleus of large atomic number [6].

Another important mapping is the Chirikov-Taylor or *standard mapping* [7; 1, Sec. 4.1B]

$$I_{n+1} = I_n + K \sin \theta_n$$
$$\theta_{n+1} = \theta_n + I_n \pmod{2\pi} . \tag{8}$$

In contrast to the Fermi map, the standard map is 2π periodic in the action I, as well as the angle. However diffusion in action can be calculated over arbitrarily many 2π periods. The standard mapping also applies to the physical systems, such as the "kicked" rotor [7] and a ball returning to an oscillating wall under the action of gravity [8,9]. Its primary importance, however is as a local (in action) approximation to mappings of form (7). For example an expansion in u about a given fixed point $u_l = M/l$, with l an integer and $\psi_l = \pi$ yields

$$\Delta u_{n+1} = \Delta u_n - \sin \theta_n ,$$
$$\theta_{n+1} = \theta_n - \frac{2\pi M}{u_l^2} \Delta u_{n+1} \pmod{2\pi} . \tag{9}$$

where $\psi_n = \pi + \theta_n$. Letting $I_n = - K \Delta u_n$, and defining

$$K = 2\pi M/u_l^2 \tag{10}$$

puts the map in the standard form (8). From (10) we see that K depends on u_l and therefore the effective K of the mapping for a given trajectory changes as it diffuses or streams. The doubly periodic nature of the standard mapping is a very important property for calculating diffusion.

The explicit mappings described above are of the class of invertible twist mappings of the form [1, Sec. 3.1]

$$u_{n+1} = u_n + \varepsilon F(u_{n+1}, \psi_n)$$
$$\psi_{n+1} = \psi_n + A(u_{n+1}) + \varepsilon G(u_{n+1}, \psi_n) \quad (\text{mod } 2\pi) \tag{11}$$

where

$$G = -\frac{\partial}{\partial u_{n+1}} \int^{\psi_n} F(u_{n+1}, \psi') \, d\psi' . \tag{12}$$

Such maps are derivable from the generating function

$$F_2 = u_{n+1}\psi_n + \int^{u_{n+1}} A(u') du' + \varepsilon \int^{\psi_n} F(u_{n+1}, \psi') \, d\psi' \tag{13}$$

and are thus area-preserving (Jacobian $J = 1$) and have a Hamiltonian form [1, Sec. 3.1]. An important special case is a radial twist map with F independent of u, such that $G = 0$, e.g., the Fermi map.

For the class of radial twist mappings, it is straightforward to construct a Hamiltonian flow using a periodic δ-function to give the kicks in action at the mapping period [3, 7; 1, Sec. 3.4]:

$$H = \int^u A(u') \, du' - \varepsilon \int^\psi F(u, \psi') \, d\psi' \sum_l \delta(n-l), \tag{14}$$

where n is a continuous time, normalized to the mapping period. For the standard mapping with the periodic δ-function in Fourier form, this becomes

$$H = \frac{I^2}{2} - K \cos \theta \sum_m e^{i2\pi mn} \tag{15}$$

where the Fourier representation of the periodic δ-function has been used. For $d\theta/dn \ll 2\pi$, an average over the Fourier components leaves only the $m = 0$ term

$$H = \frac{I^2}{2} - K \cos \theta = H_0 . \tag{16}$$

This is just the pendulum Hamiltonian

$$H = G \frac{I^2}{2} - F \cos\theta = H_0 \tag{17}$$

for the special case $F = K$, $G = 1$. The amplitude in action, of the phase space "island" associated with this motion is

$$\Delta I_m = 2(F/G)^{1/2}, \tag{18}$$

and the linearized period at the stable fixed point is

$$\Omega_0 = 26\pi/Q_0 = (FG)^{1/2}. \tag{19}$$

We will return to this formalism in the following sections.

An important radial twist mapping is the separatrix mapping which generically describes motion near the separatrix of a resonance in a system with two degrees of freedom [7; 1, Sec. 3.5]. The mapping is derived from (15) with $m=1$, by an expansion near the separatrix of (16), to obtain

$$\begin{aligned} w_{n+1} &= w_n - w_0 \sin\theta_n \\ \theta_{n+1} &= \theta_n + Q_0 \ln\frac{32}{w_{n+1}}, \end{aligned} \tag{20}$$

where

$$w_0 = 16\pi Q_0^2 \exp\left[\frac{-\pi Q_0}{2}\right], \tag{21}$$

Q_0 is the ratio of the mapping frequency to the fundamental frequency of the resonance, and w is the normalized energy deviation from the separatrix energy. The mapping (20) behaves very similarly to (7), if the action is renormalized. A local expansion in w also puts the mapping in the form (8), allowing all the results for the standard mapping to be used locally.

In addition to radial twist mappings, many physical problems lead to the more general form (11). For example, the cyclotron resonance of a charged particle gyrating in a magnetic mirror having quadratic potential and resonating with an r.f. field near the turning points in the mirror leads to a mapping of the form [4, 10]

$$E_{n+1} = E_n + AE_{n+1}^{1/3} \text{Ai}(CE_{n+1})\sin\psi_n$$

$$\psi_{n+1} = \psi_n + \frac{2\pi M}{E_{n+1}^{1/2}} + G(E_{n+1}, \psi_n),$$

where E is the perpendicular energy, ψ is the phase angle between the particle velocity and the accelerating field, $Ai(x)$ is the Airy function of argument x, A, C, and M are constants depending on the parameters, and G is obtained as in (12).

B. Structure of the Phase Space

In Fig. 2, the phase space of mapping (7) with $M = 100$ is shown schematically, with the shaded areas representing stochastic trajectories and the lines representing regular trajectories (KAM curves). The phase plane of the mapping divides naturally into three regions: (1) At velocities below u_s, the phase space is predominantly stochastic, and all period one fixed points of the map are unstable. (2) At intermediate velocities, stable islands (around elliptic fixed points) are separated from the stochastic seas by KAM trajectories; (3) At high velocities, the motion is predominantly regular, with only thin stochastic regions near the separatrices joining hyperbolic fixed points. Regions (2) and (3) are separated by a phase-spanning KAM barrier to diffusion from below, whose value averaged over phase is denoted by u_b. An analysis of linear stability at the period one fixed points gives $u_s = (\pi M/2)^{1/2}$ ($K = 4$). From the standard mapping approximation, the last KAM curve between 2π regions of the action space occurs at $K \simeq 1$ which corresponds to $u = 2u_s$ at the center of the last island structure below the first phase-spanning KAM curve (see Fig. 2).

To illustrate the form of the invariant distributions, we compare the phase space distribution of a mapping with canonical variables u, ψ, as in (7), with the more physical case of the moving wall mapping in (4). This is most easily seen for the choice $F = \sin\psi$, $F_I = -\cos\psi$. Expanding (4) to first order in F, we obtain the area-preserving mapping for the moving wall

$$E_{n+1} = E_n + 2\sqrt{E_{n+1}}\cos\theta_n \ , \tag{22a}$$

$$\theta_{n+1} = \theta_n + \frac{2\pi M}{\sqrt{E_{n+1}}} - \frac{\sin\theta_n}{\sqrt{E_{n+1}}} \ , \tag{22b}$$

which can be directly compared with (7). We illustrate the invariant distributions for these two maps in Fig. 3, for $M = 100$ and 5×10^6 iterations. A barrier to easy flow exists at $u_s = (\pi M/2)^{1/2} \approx 12.5$,

above which the distribution function falls off due to the presence of islands and higher order correlations in the phase space, with the dips near the island centers. The basic distributions for the two mappings are evident for $u < u_s$. For the moving wall mapping (22), since $f(u)du = g(E)dE$ with $g(E) = $ const and $dE = 2udu$, then $f(u) \propto u$, as observed. For the approximate mapping (7), we expect $f(u) = $ const, as observed.

The phase space for a Hamiltonian map is considerably more complicated than that immediately apparent from Fig. 2. To see this complexity we look at the standard mapping (8) for $K = 1.19$, which is slightly within the parameter range of connected stochasticity. In Fig. 4a a number of initial conditions are shown, exploring both regular (KAM) orbits and stochastic orbits. Second order island chains are seen to exist near the large island structures. In Fig. 4b, one island from a chain (inside the dashed box in Fig. 4a) is magnified, revealing a third order structure which is then magnified by the same factor to obtain Fig. 4c. This self similarity of island structures is a generic feature of a divided phase space; that is, one containing both regular and stochastic regions [12, 13].

In addition to the self similarity of the KAM island structures, there is also self similarity associated with unstable manifolds. Viewed from the four dimensional phase space, a KAM curve on the surface of section represents motion on a torus with the two angle variables specifying the coordinates on the torus. As a parameter changes such that the KAM surface no longer exists beyond a critical value, the KAM surface becomes irregular on all space scales, leading to an invariant set having an infinite number of infinitesimal gaps at the critical value. The set then has the structure of a cantor set, and has been called a *cantorus* since it originates from an invariant torus [14]. A schematic picture of the hierarchy of cantori has been developed in order to analytically calculate long-time correlations and diffusion [15]. This picture, reproduced in Fig. 5, shows the intimate relation between the island hierarchy and that of the associated cantori. The main gaps in the cantori, through which trajectories can diffuse, are indicated schematically on the figure.

For the standard map there is an additional feature that ranges of K values exist which have stable fixed points that jump by $2\pi m$, m integer, in action on each iteration [7]. These stable fixed points and their associated islands are called *accelerator modes*. Stochastic trajectories that shadow

these islands for long periods of time will tend to stream, rather than diffuse, which can result in a singularity in the diffusion coefficient [16]. For the accelerator modes of the standard map, the fixed points of a single mapping iteration are located at $I_0 = 2\pi m$, $K \sin \theta_0 = 2\pi l$ and are stable for $|2 + K \cos \theta_0| < 2$, from which we find a window of stability (in K) for

$$2\pi l < K < \sqrt{(2\pi l)^2 + 16} . \tag{23}$$

corresponding to $\pi/2 < \theta_0 < 2.1376$. The modes are born with an inverse tangent bifurcation at $K = 2\pi l$ and period double at $K = \sqrt{(2\pi l)^2 + 16}$. The first mode ($l$=1) has the largest stable range of K values and the largest maximum island size, and consequently is most important for modifying the local diffusion.

The island phase space area of the accelerator mode is found by constructing a perturbation Hamiltonian $\hat{H}$ in the neighborhood of the stable fixed point (I_0, θ_0). After averaging over the fast mapping period, as in (16), we obtain

$$\hat{H} = \frac{\tilde{I}^2}{2} + K(\cos \theta + \theta \sin \theta_0) = \hat{H}_{sx} , \tag{24}$$

where $\hat{H}_{sx}$ is the value of $\hat{H}$ on the separatrix: $\hat{H}_{sx} = K(\cos \theta_x + \theta_x \sin \theta_0)$, with θ_x the angle at the unstable fixed point. The stable island area lies within the separatrix; the island is born with zero area at one limit of stability and approaches zero area again at the other stability limit, where the stable fixed point bifurcates. The stable area is generally small and tends to go unnoticed within the stochastic sea. For more generic mappings in which K is a local function of action, the accelerator islands are not truly stable, as the changing action eventually carries the trajectories outside of the window of stability. In a generic mapping this "quasi" accelerator mode can at most locally enhance the diffusion [17]. We shall see this explicitly in the next section.

C. Diffusion Coefficient and Correlations

To describe the evolution of a distribution function $f(u, n)$ in the action alone, we assume that the change in action is small on the time scale over which the phases become random, leading to a Fokker-Planck equation for the action [18,19]

$$\frac{\partial f(u,n)}{\partial n} = \frac{1}{2} \frac{\partial}{\partial u} \left[D \frac{\partial f}{\partial u} \right],$$

(25)

where $D(u)$ is the local diffusion coefficient

$$D(u) = \frac{1}{\Delta n} \int du'(u'-u)^2 \, W_t(u,0;u',\Delta n) .$$

(26)

The transition probability $W_t(u,0;u',\Delta n)$ is the probability density that a particle has action u' at time Δn given that it had action u at time 0. The time Δn is assumed to be short compared to the evolution time of the action distribution function, but must be long compared to the phase relaxation time, such that an average over phases is implicit in (26) at fixed u. It is generally true that only the first and second moments of W_t are proportional to Δn and that transport coefficients corresponding to higher order moments vanish as $\Delta n \rightarrow \infty$. If the phases are uncorrelated over a single mapping step, we obtain directly the quasilinear diffusion

$$D_{QL} = \frac{1}{2\pi} \int_0^{2\pi} (\Delta I_1)^2 d\,\theta_0 = \frac{K^2}{2} .$$

(27)

If the phase space has structure, or the correlations are sufficient that the average over phases at fixed u for one iteration of the map is not a valid approximation, then a longer time average over both action and phase must be performed. The techniques that have been used to obtain these coefficients involve Fourier decomposition of the phase space and thus, strictly speaking, apply only to a doubly periodic phase space, obtaining a global diffusion coefficient. Two somewhat different techniques have been employed. One, called the Fourier path method, is in an efficient form for calculating higher order correlations near the border of stochasticity [20,21]. The second involves the calculation of characteristic functions that give successively higher correlations, which then must be summed to obtain the diffusion coefficient. It gives a straightforward way of calculating specific higher order correlations [22,23]. Both methods predict the same first order corrections to quasilinear diffusion. We illustrate one form of the calculation for the doubly-periodic standard map and then show how it is applied to the Fermi map.

To obtain the higher-order corrections, we calculate the diffusion coefficient

$$D_n = \frac{\langle (\Delta I_n)^2 \rangle_{I_n, \theta_n}}{n} , \tag{28}$$

in terms of the conditional probability density W that an initial state (I_0, θ_0) at $n = 0$ evolves to a final

state (I_n, θ_n) at step n,

$$D_n = \frac{1}{n} \int W(I_n, \theta_n, n \mid I_0, \theta_0, 0)(I_n - I_0)^2 dI_n d\theta_n . \tag{29}$$

W satisfies the recursion property

$$W(I, \theta, n \mid I_0, \theta_0, 0) = \int dI' d\theta' W(I, \theta, n \mid I', \theta', n-1)$$

$$\times W(I', \theta', n-1 \mid I_0, \theta_0, 0) ,$$

where, from the mapping equations,

$$W(I, \theta, n \mid I', \theta', n-1) = \delta(I - I' - K\sin\theta')\,\delta(\theta - \theta' - I' - K\sin\theta') .$$

An attempt to calculate D_n directly from (29) by repeated iterations of the mapping becomes

rapidly very tedious. Alternatively, expanding W in a Fourier series in θ and a Fourier integral in I,

we can write

$$W(I, \theta, n \mid I_0, \theta_0, 0) = \sum_m \int dq \, \exp(im\,\theta + iqI)\,a_n(m, q) , \tag{30}$$

where the Fourier coefficient a_n is also a function of I_0 and θ_0:

$$a_n(m, q) = \frac{1}{(2\pi)^2} \int d\theta dI \, \exp(-imq - iqI)(I, \theta, n \mid I_0, \theta_0, 0).$$

The evaluation of the a_n, using the recursion properties, is rather lengthy, yielding to K^{-1}, for large K

[20,21]

$$D_n = K^2[\frac{1}{2} - J_2(K) + J_2^2(K)], \tag{31}$$

where J_2 is the Bessel function of order 2. The result (without the J_2^2 term) is compared with numeri-

cally computed values in Fig. 6. The agreement is good, except where accelerator modes exist which

enhance the diffusion even on the relatively short numerical integration times. For $K < 4$, KAM

curves encircle stable fixed points. for this region the Fourier method may still be used, but the

calculation becomes increasingly tedious. An additional difficulty is the existence of non-diffusing trajectories that lie inside of the stable islands. This can be resolved by introducing a small amount of extrinsic noise, such that the result is an average over diffusing and non-diffusing trajectories. A comparison of the Fourier-path analysis, (carried out numerically) and results from iterating the mapping, for $K < 4$, is shown in Fig. 7 [20,24]. For $K < K_{crit} \approx 0.9716$, a KAM barrier exists and there is no long-time diffusion in the absence of extrinsic noise.

The Fourier path method depends on the peculiar periodicity in action of the standard map to evaluate the Fourier integrals in the limit of long times ($\Delta n \rightarrow \infty$, $D_n \rightarrow D_\infty$). Because of this, the method cannot be applied in the long time limit to maps without this periodicity. For generic maps in which the phase is randomized within a region of the action space for which the local approximation gives a near-constant K, it is possible to derive a local (in action) diffusion coefficient [24]. An expansion procedure for the Fermi map (7) gives the condition

$$(1/f)(\partial f/\partial u) \ll K(u)/2\pi. \tag{32}$$

With (32) satisfied, the diffusion coefficient for the Fokker-Planck equation (25) becomes

$$D_\infty(u) = \frac{1}{K^2(u)} D_\infty(K(u)) . \tag{33}$$

For a sharply peaked distribution, we expect good agreement only for times exceeding the time required for the distribution to broaden over many primary resonances, $n \gg 1/(K^2 D_\infty(u))$. If this n is sufficient to spread the distribution over the oscillations in $D_\infty(K)$ seen in Fig. 6, then the distribution function will be smoothed.

If we are interested in using the Fermi map to model a heating mechanism, then particles will generally start at low velocities, where the stable islands have negligibly small area. As the particles are heated they enter regions of phase space within which large islands exist. Without extrinsic stochasticity the particles will not penetrate the islands. For the ergodic phase space surrounding the embedded islands, the equilibrium distribution would be uniform. Thus to extract the diffusion of the untrapped species, alone, from the result (31) including noise, we divide that diffusion coefficient by the

fraction of phase space occupied by stochastic orbits. If we denote the stochastic equilibrium distribution by $f_s(K,I)$ normalized to one, then the relevant diffusion coefficient for the Fermi map is

$$D(u) = \frac{D_\infty(K(u))}{K^2(u) \, \langle f_s(K(u_l), I(\Delta u)) \rangle_I} \tag{34}$$

where $K(u_l) = 2\pi M/u_l^2$ and $I(\Delta u) = -K\,\Delta u$. The average over a 2π interval in I ignores rapid variations in the diffusion coefficient, which is consistent with (32).

In addition to modifying the average local diffusion, the self-similar structure of mappings with divided phase spaces gives rise to long time correlations for some particle trajectories. That is, if for some dynamical quantity one defines a correlation $C(\tau) = \langle a(t-\tau) a(t) \rangle_{initial\ cond}$, then one finds that for large τ, $C(\tau) \propto \tau^{-\eta}$ with η a constant. Numerical investigations of a related quantity, the probability that an initial phase space position in the neighborhood of an island remains in that neighborhood, gave a power law dependence

$$P(\tau) \propto \tau^{-\gamma}, \tag{35}$$

with $\gamma \approx 1.4$ for a small, isolated island [16] and $\gamma \approx 1.45$ for the standard mapping [25]. It has been shown theoretically [16] and confirmed numerically [16, 25] that $\eta = \gamma-1$. These results may not, however, be asymptotically correct [14]. The long-time correlations may be viewed physically, in terms of the properties of the phase space near KAM curves. Since orbits near KAM curves must shadow them, one would expect long time correlations from these orbits. However, as discussed in Sec. IA, the phase space in a closed region associated with such orbits must have constant density [26; 1, Sec. 3.1]. The regions in which long time correlations exist must therefore be difficult to penetrate, resulting in a decreasing number of such orbits. A quantitative calculation of this effect may be made by calculating the flux through the various cantori [14].

The real problem, however, is much more complicated. As seen in the schematic of Fig. 5, trajectories in the neighborhood of a KAM torus must penetrate through an increasingly fine grid of cantori gaps. On the way they may also be derailed to shadow a second order island chain which itself has an increasingly fine grid of cantori gaps, and so on. This infinite regressive structure leads to a tree model for calculating the flux, where computational difficulties lead to a consideration of only a few

branches of the tree. Including just the main branch and the largest island structures within the branch, a rather involved calculation gives $\gamma = 1.96$ [15]. This is clearly too large a decay rate, indicating that either higher order island structures are important for obtaining quantitatively accurate long-time correlation decay rates [15], or that the phenomenon is not captured by this theoretical picture [25].

Diffusion in generic systems is affected only slightly by long-time correlations. However there are special systems, such as those containing accelerator modes, in which the long-time correlations can have a dominant effect on the diffusion or can lead to non-diffusive transport. As discussed in Sec. IB, accelerator modes are bounded by KAM curves in a doubly periodic phase space. This is not true for maps which are not doubly periodic, in which case certain phase space regions may contain quasi accelerator modes over a finite region of action. For these quasi accelerator modes there are two mechanisms by which diffusion is enhanced: (1) Particles on locally unstable orbits become trapped on locally stable orbits within the mode as they are transported in the direction of increasing stable island size (phase space area). They then stream through values of u corresponding first to increasing and then to decreasing island size, until they are detrapped at values of u having the same island size at which they were originally trapped. (2) Trajectories near locally stable islands are only weakly unstable, and therefore shadow the stable trajectories over many mapping periods.

We estimate the effective diffusion arising from the quasi accelerator mode due to trapping and subsequent detrapping in the action (u) space, from the relation

$$D_T \approx \frac{(\Delta u)^2}{2\tau} g(K)$$

(36)

where τ is the average streaming time, Δu is the average distance over which streaming takes place, and $g(K) = A_I(I)/(2\pi)^2$ is the fraction of participating phase space, with A_I the stable island area. Since for a single iteration I steps by $2\pi I$, $\Delta I = 2\pi/\tau$ and $\Delta u = \tau$. Using A_I calculated at the center of the stable range of K, from the island Hamiltonian in (24) we obtain [17]

$$g(K) = \frac{1}{(2\pi)^2} \frac{24}{5} \frac{8^{5/4}}{K^2} ,$$

(37)

and from the equilibrium condition (10) we obtain, by differentiation,

$$\Delta u = \frac{(2\pi M)^{1/2}}{2K^{3/2}} \Delta K . \tag{38}$$

From (23) we find the value of $\Delta K = K - 2\pi l$ at the middle of the mode to be $\Delta K = 4/K$. Substituting this into (38) and using (37) and (38) in (36) gives

$$D_T \approx \frac{(2\pi M)^{1/2}}{K^{5/2}} \frac{24}{5} \frac{8^{5/4}}{(2\pi)^2 K^2} . \tag{39}$$

We can compare the value and the scaling of D_T in (39), with the value obtained from the long-time correlations, but ignoring the trapping and detrapping. To do this we use the result for the correlation time of (35) with $\gamma = 1.4$ to estimate the part of the diffusion coefficient due to long time correlations near but outside of the accelerator mode as

$$D_c = \int_{}^{\tau_{max}} \frac{(\Delta u)^2}{2\tau} P(\tau) g(K) d\tau . \tag{40}$$

Using $\tau_{max} = \Delta u$ in (40), assumed large, the integration of (40) gives

$$D_c = \frac{8}{3} \left[\frac{(2\pi M)^{1/2}}{K^{5/2}} \right]^{0.6} \frac{24}{5} \frac{8^{5/4}}{(2\pi)^2 K^2} . \tag{41}.$$

Comparing (39) with (41) we note that, except for a numerical factor of order unity, the two expressions differ only in that the factor $(2\pi M)^{1/2}/K^{5/2}$ is taken to the 0.6 power in (41), while it is linear in (39). Since this factor is assumed large for the effect of the quasi accelerator mode to be important, we conclude that the trapping and detrapping dominates the effect of correlations. However, the requirement that $(2\pi M)^{1/2}/K^{5/2} \gg 1$ puts a severe requirement on the local uniformity (size of M) for the effect of the quasi accelerator mode to be significant. For example, for the lowest mode with $K = 2\pi$, we require that $M \gg 1.5 \times 10^3$. The higher modes (in l) become increasingly dependent on having a large value of M, in order to result in significantly enhanced diffusion.

A two degree of freedom Hamiltonian system can exhibit somewhat different properties from those described above when the two unperturbed frequencies are widely different. For example, consider $H(p, q, \Omega t)$ with H periodic in $\lambda = \Omega t$ and Ω small. Fixing λ, a transformation of H to

action angle form yields the action $J(H)$. In the limit of $\Omega \to 0$ there is a separation of orbits such that for those orbits not crossing a separatrix the action is constant to all orders in Ω, while for separatrix crossing orbits the motion is strongly chaotic. This leads to a sharply divided phase space, rather than the typical phase space with intermingled regular and chaotic orbits shown in Figs. 2 and 4. For this case the jump in action due to separatrix crossing and the consequent diffusion has been calculated in [27-30]. The general formulas are complicated, so we illustrate the results here for the case of symmetric separatrix crossings only. An example is the Hamiltonian system

$$ H = \frac{p^2}{2} - A(t)\cos x \; , \tag{42} $$

where A is periodic in Ωt with period 2π and is slowly varying in that $\dfrac{1}{\omega_o}\dfrac{d\ln A}{dt} \ll 1$ for all A, where $\omega_o = A^{1/2}$ is the frequency for deeply trapped orbits. Letting $A = 1 - a\cos\Omega t$ with $|a|<1$, we can rewrite (42) in the form

$$ H = \frac{p^2}{2} - \cos x + \frac{a}{2}\left[\cos(x+\Omega t) + \cos(x-\Omega t)\right] \; , \tag{43} $$

which shows the equivalence to the general form (14) if we do not take ε to be small. The separatrix action for (42) is $J_{sx} = 8A^{1/2}$. The appropriate mapping representation has a period $T = \pi/\Omega$ for separatrix crossings from rotation to libration or the reverse. For those orbits, the phase-averaged mean square deviation in the action can be calculated to be [29,30]

$$ \langle(\Delta J)^2\rangle = \frac{(\pi \dot{J}_{sx}/\omega_o)^2}{12} \; , \tag{44} $$

where $\dot{J}_{sx}$ is evaluated at the separatrix crossing for a given action J. For Hamiltonian (42) this yields $\langle(\Delta J)^2\rangle = \frac{4}{3}\pi(\frac{\dot{A}}{A})^2$ and consequently the quasilinear diffusion coefficient

$$ D = \frac{\Omega\langle(\Delta J)^2\rangle}{\pi} \propto \Omega^3 \; , \tag{45} $$

which is very slow in the "adiabatic" limit $\Omega \to 0$.

D. Phase Space Transport

In solving the Fokker-Planck equation to obtain transient or steady-state distribution functions, particle flow rates from sources to sinks, or energy deposition, the main determining factors are the variation of local D_{QL} with action (random phase assumption), the boundary conditions, and the effect of correlations on D. For a steady-state problem the higher order correlation corrections to D usually make minor changes to the relevant quantities. Clearly large islands in the phase space will make some difference, as they exclude significant phase space from the diffusive process. However, the long-time correlations near the edges of the islands usually have negligible effect on the diffusion. This is because it is the fastest diffusing particles that dominate the overall diffusion. The one exception is for quasi accelerator modes, in which it is the longest correlated trajectories that are the fastest diffusing. In addition, near the transition at which phase spanning KAM curves are just broken, the existence of not easily penetrated cantori make calculation of the corrections to quasilinear diffusion important. In both of these instances, in order to include the correlation corrections, a generic mapping must be locally approximated by the standard mapping (or its equivalent) over many fixed points; e.g., the Fermi map with large M.

As an example of the effects of correlations and embedded KAM islands, we return to the Fermi map (7) with diffusion coefficient (34). For the ergodic phase space surrounding the islands, the equilibrium invariant distribution is uniform. However, because the chaotic motion does not enter the islands, the phase-averaged invariant distribution $f_s(u)$ is not uniform, but has dips in the regions of u where islands exist (see Fig. 3). The observed distribution function $F(u,n)$ is then related to the solution of the Fokker-Planck equation $f(u,n)$ by

$$F(u,n) = \frac{f(u,n)f_s(u)}{\int_0^{u_b} f(u',n)f_s(u')du'} \tag{46}$$

where $\int_0^{u_b} F\, du = 1$. Clearly as $n \to \infty$ and $f(u,n)$ becomes uniform, $F(u,n) \to f_s(u)$.

In addition to comparing $F(u,n)$ directly with distributions obtained by iterating the mapping equations, it is useful to calculate the second moment or variance of $F(u,n)$. This variance can be

compared to the variance measured by iterating the map. That is, we compare the measured value of the variance σ_x^2 to the theoretical value

$$\sigma_t^2(u_0, n) = \frac{1}{n} \frac{\int (u - u_{ave})^2 F(u, n) du}{\int F(u, n) du} , \qquad (47)$$

where

$$u_{ave}(u_0, n) = \frac{\int u F(u, n) du}{\int F(u, n) du} .$$

We integrate the Fokker-Planck equation using the theoretical diffusion coefficient (34) and a delta function at action u_0 as an initial condition. This yields the predicted theoretical distribution function $f(u, n)$, where the dependence on the initial action u_0 is suppressed. The final distribution function is obtained as in (46).

The mapping equations were solved numerically, and compared to the time-dependent Fokker-Planck solution, with the results given in Fig. 8. For the case chosen of $M = 10,000$, Fig. 8a corresponds to initial conditions in the essentially stochastic phase space below u_s and Fig. 8b corresponds to initial conditions in the stochastic sea between u_s and u_b. In Fig. 8a we note that the distribution is not symmetric due to the inhomogeneity of $D(u)$ given in (34). The theory and experiment are in good agreement. The bump in the distribution obtained in the numerical experiment at 100 $< u <$ 105 is due to the quasi accelerator mode at $K = 2\pi$. In Fig. 8b, since there were no initial conditions inside the island centered at $u = 185$, the island manifests itself as a dip in the distribution function. Evidence of neighboring period one islands may be seen on the skirts of the distribution function at $u = 189$ and $u = 182$. The effects of the two iteration islands at $u = 183$ and $u = 187$ are also visible.

The numerical variance was also calculated, using

$$\sigma_x^2(u_0, n) = \frac{1}{nm} \sum_{i=1}^{m} (u_i(n) - u_{ave})^2 . \qquad (48)$$

The results after an iteration time $n = 20$ are shown as dots in Fig. 9. The solid line obtained by integrating the Fokker-Planck equation is a linear interpolation of several hundred calculatons of the

variance, each at a different initial u_0. The variances in Fig. 9 both show the characteristic oscillations for $K > 4$ and fall to zero as K approaches one, as in the standard map. However, the oscillations for the Fermi map occur in action space rather than in parameter space. For $u < 40$, both the theoretical and measured variances no longer exhibit oscillations. This is because diffusing particles experience different local diffusion rates which average the rapid variations in $D(u)$ to the quasilinear value of 1/2.

We can estimate the range of u for which the quasilinear diffusion coefficient can be used. We expect that quasilinear diffusion is adequate if large islands do not exist ($u < u_s$) and if particles diffuse over a range of action Δu comparable to or larger than the local period of the oscillations in $D(u)$. For large K the diffusion oscillates as $\cos K$ so we expect averaging when $(\partial K / \partial u) \Delta u \approx \pi/2$. Using $\Delta u \equiv \sqrt{n D_{QL}}$ and $\partial K / \partial u = 4 \pi M / u^3$ for the Fermi map, we find quasilinear diffusion for

$$u < (32 M^2 n)^{1/6} \leq u_s . \tag{49}$$

The validity of (49) has been studied numerically for $10^2 < M < 10^8$ and $10 < n < 1000$. For actions satisfying (49), the variance is within five percent of the quasilinear value [24].

For actions greater than $u \approx 200$, i.e., for actions near u_b, the numerically determined values of the variance exceed the theoretical values. Initial conditions near an isolating KAM curve around a stable fixed point tend to "stick" to the island border, being carried around the island. This effect produces an anomolous variance which decays as $1/n$. As $n \to \infty$ we expect that the numerical variance will agree with the theoretical predictions. Numerically iterating the mapping equations for longer times verifies this $1/n$ decay. In calculating the variances, only initial conditions outside of stable islands are selected. This is straightforward for period one fixed points, but increasingly difficult for higher order fixed points. Initial conditions started in such islands also produce variances which decay as $1/n$, leading to a numerical variance lower than that calculated from the Fokker-Planck equation, as was observed numerically.

We now discuss quasi accelerator modes in greater detail, showing how their effect can be included, for generic maps, within a Fokker-Planck formalism. To treat the distribution locally, we consider the streaming explicitly as sources and sinks in the Fokker-Planck equation. This is a natural

description when only the more important trapping-detrapping mechanism is considered. The diffusion coefficient is then that of the non-streaming particles, as previously obtained in (33). The Fokker-Planck equation, including sources and sinks, can be written

$$\frac{\partial f}{\partial t} = \frac{\partial}{\partial u} \left[\frac{1}{2} D(u) \frac{\partial f}{\partial u} \right] + S(u) - L(u) \ . \tag{50}$$

The sources and sinks are straightforwardly determined, in principle, from the amount of phase space captured or lost from the islands. Since there are two symmetric islands at a given u in the mode near $\theta = \pm \pi/2$, transporting phase space in opposite directions, the loss and source terms are closely related, as $L = a'(u)f(u,n)$, $S = a'(u)f(\overline{u},\overline{n})$, where $a'(u) = |A'(u)/2\pi|$ and $A'(u)$ is the derivative with respect to u of the island area $A(u)$. The barred quantities are defined by $A(\overline{u}) = A(u)$, and, for the steady-state, f is independent of n. Taking A' antisymmetric about some maximum value A_m, at u_m, making the change of variable $u = u_m - x$, $\overline{u} = u_m + x$, we expand $f(u)$ and $f(\overline{u})$ in Taylor series about $u = u_m$ to obtain

$$S - L = a'(x)f'(0)2x \ . \tag{51}$$

Substituting (51) into the Fokker-Planck equation (50), we have, in the variable x

$$\frac{1}{2} \frac{d}{dx} D \frac{df}{dx} + a'(x)f'(0)2x = 0 \ . \tag{52}$$

To obtain a solution of (52) we need to have explicit expressions for $D(u)$ and $A(u)$. In general, these are complicated functions allowing only numerical calculations. The result of these calculations for the total stable area of the lowest accelerator mode versus K is shown in Fig. 10. The structure of the mode is qualitatively understood in terms of the various resonances, which are indicated on the figure. The initial mode area growth versus K is similar to that expected, (dash-dot curve) but decreased due to the growth of the stochastic layer near the mode separatrix. The first major dip in the regular area near $K \approx 6.6$ involves the 4:1 resonance between the mapping and local island frequencies. The growth of this island chain and its interaction with other second order islands rapidly increases the stochasticity within the separatrix of the main island. At the bottom of the dip in area most of the stable area lies in the 4-island chain, rather than in the main island. The reestablishment of

the stable area near $K \approx 6.7$ is achieved by restabilization of the central island, as the 4-island chain moves outward. The first extinction of the stable island occurs due to a very strong 3:1 resonance interaction near $K \approx 7.0$. Again, the 3-island chain moves outward, reestablishing the central stability region. The 2:1 resonance, which is the period doubling bifurcation of the central fixed point, appears at $K \approx 7.4$, followed by the usual period doubling sequence to chaos. The dashed curve is the analytic approximation to match the integrated area under the island area curve for use in (52). Because the solution of the Fokker-Planck equation depends only on $\int_0^{\Delta u} a dx$, the exact form of the variation of the island area is of little importance.

For comparison of the analytic solution of (52) with numerical simulations, a source and sink were placed on opposite sides of the mode, and flux continuity was required [17]. As suggested by the requirement that M be large, as given previously, $M = 10^7$ was used for computations near the first quasi accelerator mode ($K \approx 2\pi$). To insure continuity of flux, we match the theoretical and numerical slope to $1/D(u)$, from (31), at the value of u for which the mode is born by an inverse tangent bifurcation ($K = 2\pi$). The comparison of theory and experiment is shown in Fig. 11. We see that the fit is quite reasonable for that portion of the mode in which the stable island is growing or nearly constant.

II. Dissipative Systems

A. Phenomena in Dissipative Maps

We consider chaotic motion in weakly dissipative twist maps of the form

$$
\begin{aligned}
y_{n+1} &= y_n + \varepsilon F(x_n, y_{n+1}, \delta) \\
x_{n+1} &= x_n + A(y_{n+1}) + \varepsilon G(x_n, y_{n+1}, \delta)
\end{aligned}
\tag{53}
$$

where F and G are periodic in x with period 2π, δ is the dissipation strength, and $z = (x, y)$ become the angle-action variables for the unperturbed ($\varepsilon = 0$) Hamiltonian system. The Fokker-Planck equation for the phase-averaged distribution can be written as

$$
\frac{\partial f}{\partial n} = -\frac{\partial}{\partial y}(Bf) + \frac{1}{2}\frac{\partial}{\partial y}\left[D \frac{\partial f}{\partial y}\right],
\tag{54}
$$

where $D(y)$ is the diffusion coefficient for the underlying Hamiltonian part of the perturbation, and $B(y)$ is the friction coefficient due to the dissipative part. The diffusion coefficient D is determined, setting $\delta = 0$ in (53), as in (26). Considering δ as perturbative, the friction coefficient can be determined using the random phase assumption

$$B(y) = \frac{\varepsilon}{2\pi} \int\limits_{0}^{2\pi} dx \, [F(x,y,\delta) - F(x,y,0)] \, . \tag{55}$$

Some early studies of transient chaos in dissipative maps were reported in references [2,31,32]. In [31,32] the authors considered a quadratic map on a 2-torus

$$p_{n+1} = \{p_n + Kg(x_n) - \delta(p_n - \frac{1}{2})\} \, , \tag{56a}$$

$$x_{n+1} = \{x_n + p_{n+1} - \frac{1}{2}\} \, , \tag{56b}$$

where $g(x) = x^2 - x + \frac{1}{6}$ and the brackets $\{ \}$ denote modulo 1. This map has a Jacobian $1 - \delta$, where δ is the dissipation parameter. For the Hamiltonian limit $\delta = 0$ with $K \gg 1$, the phase space ($0 \leq p < 14$, $0 \leq x < 1$) is found to be mostly chaotic, with small embedded islands. For weak dissipation $\delta \ll 1$, the chaotic motion becomes transient, and all initial conditions ultimately are attracted into embedded islands. As δ is increased from 0, the mean rate of decay $\overline{\alpha}$ over an ensemble of initial conditions from the transiently chaotic region of phase space at first increases, and then decreases again as δ approaches a critical value δ_{cr}. For $\delta > \delta_{cr}$, $\overline{\alpha} = 0$ and persistent chaos on a strange attractor appears.

This early study illustrates the two types of behavior that are observed in the regime of transient chaos: (1) For weak dissipation, $0 < \delta < \delta_s$, the mean rate of decay $\overline{\alpha}$ of the chaotic transient, averaged over an ensemble of initial conditions, is an increasing function of δ. The transient behavior in this case is determined by the underlying Hamiltonian dynamics and the rate of phase space contraction $1 - \delta$. (2) For $\delta_s < \delta < \delta_{cr}$, $\overline{\alpha}$ decreases with δ and tends to zero as $\delta \to \delta_{cr}$. This behavior is dominated by a boundary crisis [33] in which, as $\delta \to \delta_{cr}$, all stable periodic orbits of the map are "disconnected" from the underlying strange attractor, which exists for $\delta > \delta_{cr}$. A rescaling argument is used

to determine the transient behavior in this case. We consider these two cases separately.

B. Transient Chaos with Weak Dissipation

For $0 < \delta < \delta_s$, the estimate

$$\overline{\alpha} \approx A \delta , \tag{57}$$

has been made [32], where $A(K)$ is the fraction of the total phase space area occupied by the stable islands in the underlying ($\delta = 0$) Hamiltonian system. This estimate can be understood as follows: In one iteration of the map, the area of each stable island A_k is reduced by the amount of δA_k. Because $K \gg 1$, we can assume that the area of the chaotic region of phase space is unity and that the distribution of phase points in the chaotic region is uniform. Then a fraction $\sum_k A_k \delta = A \delta$ of the initial conditions in the chaotic region are captured by the islands each iteration, giving (57).

Another example that has been studied [34-36] is the Henon map [37], restricted to a 2-torus:

$$x_{n+1} = [y_n + d + ax_n^2] \tag{58a}$$

$$y_{n+1} = [bx_n] . \tag{58b}$$

Here [ ] denotes modulo-4; i.e., $|x| \leq 2$ and $|y| \leq 2$. The Jacobian of this map is $-b$. For the case $d \neq 0$, (57) for the mean decay rate $\overline{\alpha}$ of the transient chaos was verified numerically for $a = 1$, $\delta = 1 - |b| = 0.01$, 0.02 and 0.05, and $0.1 \leq d \leq 1.0$. Furthermore, $\overline{\alpha}$ was found to decrease rapidly as δ approached some critical value δ_{cr}. For $\delta > \delta_{cr}$, a strange attractor was observed.

A variation of (57) results when the Jacobian of the map is not a constant over the phase space. An example where this arises is the nonuniformly-sampling, digital phase-locked loop [38,39]. The mapping equations for this system on the 2-torus are

$$I_{n+1} = \{I_n - r \delta \sin\phi_n + \delta \sin(\phi_n - I_n)\} \tag{59a}$$

$$\phi_{n+1} = \{\phi_n + I_{n+1}\} \tag{59b}$$

where { } denotes modulo-2π. The Jacobian is

$$J = 1 - \delta \cos (\phi - I) \tag{60}$$

and can be less than or greater than one depending on the phase space coordinates. This map was stu-

died numerically for $0.58 \leq \delta \leq 0.85$ and $3.5 \leq r \leq 4.5$. Over this parameter range the phase space contains a single large stable island with an attracting fixed point at $I = 0$, $\phi = 0$. The local value of the Jacobian is $1 - \delta$ at the fixed point. For a grid of 100×100 initial conditions, transient chaotic behavior was observed numerically. The number of phase points undergoing transient chaotic motion decays exponentially with iteration number n, having mean decay rate $\overline{\alpha}$.

To find $\overline{\alpha}$ analytically, the underlying Hamiltonian map near the $I = 0$, $\phi = 0$ must be determined by expanding the term $\delta \sin(\phi_n - I_n)$ in (59a) in I_n. The lowest order part, independent of I_n, may be combined with the remaining mapping to give

$$I_{n+1} = I_n - (r-1)\, \delta \sin \phi_n \tag{61a}$$

$$\phi_{n+1} = \phi_n + I_{n+1}\ , \tag{61b}$$

which is the standard map with stochasticity parameter $K = (r-1)\,\delta$. A grid of 25×25 initial conditions yields the typical surface of section shown in Fig. 12, consisting of a large stable island surrounded by a stochastic sea. The stable island area A can be found either numerically or analytically. It was found [40,41] that in an average sense the stable area could be reasonably approximated for $1 < K < 6$ by

$$A = \frac{1}{2}\, A_0 K^{-1.3} \tag{62}$$

where $A_0 = 4\,\pi^2$ is the entire area of the phase space.

Assuming, as for (56), that the distribution in the region of transient chaos is uniform and that the decay is exponential with n, we can estimate that in one iteration the island will capture a fraction of phase points $\overline{\alpha}$ given by

$$\overline{\alpha} = -\ln\left[1 - \frac{\delta A}{A_0 - A}\right]\ . \tag{63}$$

This expression for $\overline{\alpha}$ is similar to that given by (57) except that the local contraction rate at the island center is used, and the rate $\overline{\alpha}$ is not assumed to be much less than unity. A typical case studied was $r = 4.0$, $\delta = 0.688$, such that $K = 2.06$. The measured decay rate was 0.15/iteration, and the theoretical decay rate from (63) was 0.18/iteration. For the thirteen cases studied [39], the measured decay rate

was typically within 20% of the theoretical decay rate over the entire range of parameters.

It is often not the case that the action variable [p in (56)] is defined on a torus. In this case the distribution f is a function of action and δ and is not uniform in action. The behavior of the chaotic transient can still be determined using the basic idea that the stable islands capture a certain fraction of initial conditions each iteration. Now, however, the fraction of initial conditions captured by each island depends on the value of the distribution function near that island. The distribution can be determined from the Fokker-Planck equation by including the effects of dissipation.

The calculation procedure can be illustrated using as an example the dissipative Fermi map [42-44, 35]. The dissipation is introduced by assuming that the ball suffers a fractional loss δ in velocity upon collision with the fixed wall. The map is then

$$\overline{u} = (1-\delta)u_n - \sin\psi_n \ . \tag{64a}$$

$$\overline{\psi} = \psi_n + 2\pi M/\overline{u} \ , \tag{64b}$$

$$(\psi_{n+1}, u_{n+1}) = (\overline{\psi}, \overline{u})\,\text{sgn}\,\overline{u} \ , \tag{64c}$$

The function $\text{sgn}\,\overline{u} = \pm 1$ for $\overline{u}$ positive or negative, respectively, is introduced to maintain $u_{n+1} \geq 0$ for low velocities $u_n < (1-\delta)^{-1}$, while preserving the continuity of the map near $u = 0$. The Jacobian of the map is $1 - \delta$, and thus the map is area preserving for $\delta = 0$. The primary fixed points of the map are found by setting $u_{n+1} = u_n$ and $\psi_{n+1} = \psi_n$ (mod 2π) in (64), to obtain

$$(u_k, \psi_k) = (M/k, \sin^{-1}(-u_k\delta)) \ , \tag{65}$$

where k is an integer. As in the Hamiltonian map there are two fixed points for each k at $\psi_k \approx 0$ and $\psi_k \approx \pi$, for $u_k\delta \ll 1$, with $\psi_k \approx \pi$ stable for $u_k > u_s = (\pi M/2)^{1/2}$ and $\psi_k \approx 0$ always unstable.

We summarize the behavior of the motion, determined by numerical iteration, as the parameters M and δ are varied. For $\delta = 0$, there is no dissipation and the usual Hamiltonian chaos ensues, as described in Part I. For weak dissipation, $0 < \delta < \delta_c$, the fixed points of the Hamiltonian map become attractors (sinks), and all persistent chaotic motion is destroyed. However, transient chaotic motion surrounds the sinks below u_b. As an example, for $M = 30$ ($\delta_c \approx 0.02$) and $\delta = 0.003$, we find that an initial phase point chosen randomly below u_s undergoes transient chaotic motion for a mean number of

iterations $\bar{N} \approx 13000$ before it enters an embedded island between u_s and u_b and becomes trapped in an island sink. For eleven cases studied numerically [35], the decay from the transiently chaotic region is observed to be exponential at a rate $\bar{\alpha} = \bar{N}^{-1}$.

In Fig. 13 we plot the cumulative phase-integrated distribution

$$\bar{f}(u) = 100 \int_0^N dn \int_0^{2\pi} d\psi f(u,\psi,n) .$$

for $M = 30$, $\delta = 0.003$, after $N = 5 \times 10^4$ iterations, for 100 initial conditions at low velocities chosen randomly. We see evidence of attracting sinks between u_s and u_b near the primary resonances at $k = 3$ (a period-1 and a period-5 sink coexist) and at $k = 4$ (a period-1 and a period-3 sink coexist). The density leaving the stochastic region flows into these sinks, forming spikes in the figure. For all cases studied, the location and structure of these sinks correspond to the Hamiltonian ($\delta = 0$) structure of the stable fixed points (65) of the Fermi map. The period-3 and period-5 sinks correspond to secondary fixed points encircling the period-1 primary fixed points [1, Sec. 2.4].

For sinks occupying a sufficiently small fraction of the phase space and $f \ll 1$ we might expect that the phase-averaged distribution function outside of the island sinks could be represented approximately as a quasistatic distribution

$$f(u,n) = f_Q(u) \exp(-\bar{\alpha}n) \tag{66}$$

where f_Q is the steady state solution to the Fokker-Planck equation (54) with $D(u)$ given approximately as in (26) and $B = -u\delta$ given from (55). Because the Fokker-Planck equation averages over small scale oscillations in D, as seen in Fig. 9, we can approximate $D \approx 1/2$, the quasilinear value, for $u < u_s$, and we note that D falls to zero at $u = u_b$. A reasonable estimate over the entire range $0 < u < u_b$ has been found to be [35, 44]

$$D = \frac{1}{2}(1 - u^2/u_b^2)^2. \tag{67}$$

Using these values in (54), with the quasi-steady-state assumption that the net flux is zero, we obtain

$$f_Q(u) \propto \exp[-2\beta u^2/(u_b^2 - u^2)]. \tag{68}$$

This distribution, scaled to the value of $\bar{f}$ at $u = 0$, is plotted as the dashed line in Fig. 13 for

$M = 30$ and $\delta = 0.003$. Equally good agreement is found for all other cases studied.

We can also determine the phase-space area ΔA_k in the transiently chaotic region that is captured by each primary island during one iteration. Using the standard map (with $\delta = 0$) to calculate the stable area $\overline{A}$ in (I, θ) variables surrounding the single iteration fixed point at each k, then for $\delta > 0$, $\overline{A}$ contracts by the factor $1 - \delta$. Thus $\Delta \overline{A} = \overline{A}\delta$. Transforming back to (u, ψ) variables, the phase-space area for each stable fixed point is

$$\Delta A_k(u_k) = \overline{A}\delta/K$$

where $\overline{A}$ is a function of $K = u_b^2/u_k^2$ given by (62). The decay rate for the transiently chaotic region is then estimated as

$$\overline{\alpha} = \sum_k \alpha_k, \tag{69a}$$

where

$$\alpha_k = f_Q(u_k)\Delta A_k \tag{69b}$$

and the sum is over all stable primary fixed points u_k in the region $u_s < u < u_b$.

The numerical and analytical values of the decay rate $\overline{\alpha}$ have been compared for eleven cases spanning the parameters $0.0003 \leq \delta \leq 0.01$ and $30 \leq M \leq 300$. The theory and experiment typically agree to within a factor of two. As examples, for $\delta = 0.01$ and for $M = 300$, $\overline{\alpha} = 1.1\times10^{-5}$ numerically, and $\overline{\alpha} = 0.9\times10^{-5}$ analytically. For $M = 30$, the corresponding values are $\overline{\alpha} = 2.7\times10^{-5}$ and 6.6×10^{-5}, respectively. The large deviation in the second case is mainly due to local significant variation from the approximation (62) of the stable area, as we have seen for the quasi accelerator mode islands in Fig. 10. Deviations from the theoretical invariant distribution due to the approximation (67) also contribute. The fraction $\mu_k(=\alpha_k/\alpha)$ of initial phase points that ultimately stick to the various main-island fixed points (including their secondary fixed points) can also be found analytically with use of (69) [1, Sec. 4.3; 35].

A local, but more complete description of transient chaos has been put forth by various authors [45-50]. Because the number of phase points in a region of transient chaos decays exponentially with iteration number n, there exist initial conditions having arbitrarily long, transiently chaotic trajectories.

Each such limiting trajectory is a fractal object having zero measure, which can be called a "chaotic repeller," and which is part of the boundary of the basin of the (nonchaotic) attractor. On each of these "repellers" embedded in phase space, one generally finds a unique invariant distribution and one can define topological and metric entropies, Lyapunov exponents and various fractal dimensions, just as these are defined for the persistent chaos on a "strange attractor." In some cases, initial conditions that are "close" to a chaotic repeller are immediately repelled. In other cases, nearby initial conditions are first attracted to the repeller, and repulsion occurs at much latter times, in directions transverse to the attracting ones. Such chaotic repellers may be called "chaotic semi-attractors."

For a repeller in a one dimensional map, such as the quadratic map [1, Sec. 7.2]

$$x_{n+1} = C - x_n^2,$$

it is proposed in [49] that the decay rate α of the chaotic transient near a repeller can be written

$$\alpha = (1 - D)\lambda, \tag{70}$$

where D is the information dimension [51] and λ is the (positive) Lyapunov exponent on the repeller. Expression (70) for the decay rate α can be understand as follows: partition an interval l covering the repeller into equal subintervals of length $\varepsilon \ll l$. The number M of subintervals required to cover the repeller within l is $M(\varepsilon) = M_0 \varepsilon^{-D}$, where D is the fractal dimension. The total length of these subintervals is $l_R = M_0 \varepsilon^{1-D}$. After one iteration, the interval l is mapped to a new interval l' that covers the repellers, and the interval and subintervals are increased in length by the factor e^{λ}, where λ is the Lyapunov exponent. Subintervals having length $\varepsilon e^{-\lambda}$ within l are mapped to subintervals having length ε within l'. The total length of the subintervals within l that lie on the repeller within the interval l' is

$$l_R' = M(\varepsilon e^{-\lambda})\varepsilon = M_0 \varepsilon^{1-D} e^{\lambda D}$$

Thus after one iteration, the fraction $e^{-\alpha}$ of phase points remaining on the repeller is

$$e^{-\alpha} = \frac{l_R'/l'}{l_R/l} = e^{-\lambda(1-D)},$$

and (70) immediately follows.

Generalizing to higher dimensional systems, one may write

$$\alpha \;=\; \sum_{i=1}^{d}{}' \lambda_i (1 - D_i) \tag{71}$$

where the D_i are the information dimensions along the directions defined by the d Lyapunov exponents λ_i, and the sum is over the unstable directions ($\lambda_i > 0$) only. The decay rate (71) has been verified for three different 2-dimensional maps [49].

Returning to the map (56), we illustrate this behavior in Fig. 14 (reproduced from [49]), showing the attractors and repellers for $K = 3.5$ and $\delta = 0.1$. The heavy dots represent a stable period-6 cycle, whose attractor basin is extremely small. The main attractor is the fixed point marked by a cross. The four-fold structure around this fixed point is a semi-attractor, consisting of a chaotic period-4 cycle. Phase space in its neighborhood is attracted rapidly onto the structure and is then repelled, leading to a decay of the density given by (71) with $\alpha = 0.00548$. Figure 14 also shows a repeller characterized by the dots scattered all over the figure. Trajectories escape from this repeller by either going directly towards the fixed point, or by being attracted first towards the semi-attractor, with the latter found to be the more frequent. The decay rate of the large repeller was found to be $\alpha' = 0.047 \pm 0.004$. If we assume that almost all the phase space from the large repeller is first attracted to the semi-attractor then the two structures are in series. The average life time of the chaotic transient is then the sum of the individual life times,

$$T \;=\; \frac{1}{\alpha} + \frac{1}{\alpha'} \;=\; 204 \pm 3.$$

In general, the repeller structure may be very complicated, with repellers and semi-attractors connected in complicated patterns. This is particularly true in weakly dissipative systems, where many interwoven basins of attraction exists, each having their own connections to local repeller structures. It is presumably the combination of these complicated local structures that yield the overall global decay rate, which must be equivalent to the absorption rate into the sinks, as calculated from (69).

C. Transient Chaos near a Crisis

In the regime $\delta_s < \delta < \delta_{cr}$, the transient behavior is dominated by a boundary crisis [33]. The

decay rate $\bar{\alpha}$ tends toward zero as δ approaches δ_{cr}, and a strange attractor exists for $\delta > \delta_{cr}$. For values of δ slightly below δ_{cr}, it is often found [33] that

$$\bar{\alpha} \sim (\delta_{cr} - \delta)^{\gamma}$$

where γ is the critical exponent of the chaotic transient.

The one-dimensional quadratic map exhibits this behavior near the critical value $C_{cr} = 2$. For $C < C_{cr}$, a chaotic attractor exists over the range $-x_1 < x < x_2$, which itself lies within a basin of attraction $-x_* \leq x \leq x_*$, where

$$x_* = \frac{1}{2} + (\frac{1}{4} + C)^{1/2} \tag{72}$$

and where $-x_*$ is the location of the unstable fixed point of the map. As $C \to 2$, $-x_1 \to -x_*$, the strange attractor collides with its basin boundary (the "crisis") and is destroyed. For $C > 2$, the region $-x_1 < x < x_2$ formerly occupied by the chaotic attractor is a region of transient chaos, with the orbit ultimately tending to an attractor at $x = -\infty$. The decay rate of the chaotic transient is found to scale as

$$\bar{\alpha} \sim (C - C_{cr})^{1/2}. \tag{73}$$

As pointed out in [46], this scaling results because, for $C > C_{cr}$, there is an escape region $|x| < (C - x_*)^{1/2}$ within the region of transient chaos, which first maps into $x > x_*$, then maps into $x < -x_*$, and thereafter on repeated iteration to the attractor at $x = -\infty$. Writing $C = C_{cr} + \Delta C$ and using (72), we obtain

$$|x| < \left[\frac{2}{3}(C - C_{cr}) \right]^{1/2}$$

for the size of the escape region, and the scaling (73) immediately follows.

Similar phenomena are observed in higher dimensions [46, 33]. There appear to be two possible crises in strictly dissipative ($J < 1$ everywhere) two dimensional maps. These are illustrated in Fig. 15. In (a) the stable manifold of an unstable periodic orbit (B) on the basin boundary collides with the unstable manifold of an unstable periodic orbit (A) on the strange attractor. In (b), the stable and

unstable manifolds of an unstable periodic orbit (B) on the basin boundary collide. In both cases, the chaotic attractor is the closure of the branch of the unstable manifold of (B) that points into the basin of attraction. The critical exponent for crises of type (a) can be written

$$\gamma_a = \frac{1}{2} + (\ln |\lambda_1|)/|\ln |\lambda_2||$$ (74a)

and of type (b),

$$\gamma_b = (\ln |\lambda_2|)/(\ln |\lambda_1 \lambda_2|^2).$$ (74b)

Here, λ_1 and λ_2 are the contracting and expanding eigenvalues, respectively, of the periodic orbits A or B.

Equations (74a) and (74b) have been verified for the Henon map (58) [but not restricted to a torus]. For $a = -1$, $b = 0.3$, there is a crisis of type (a) at $d_{cr} \approx 1.4269$. For $a = -1$, $b = -0.3$, there is a crisis of type (b) at $d_{cr} \approx 2.1247$. Plotting log $\overline{\alpha}$ versus log $(d - d_{cr})$ from numerical results obtained by averaging 300 initial conditions for each value of d, one finds a straight line whose slope γ is in good agreement with (74a) and (74b) respectively.

D. Persistent Chaos and Invariant Distributions

For area-preserving maps, the invariant distribution on any chaotic subset in the surface of section is trivially a constant. For chaotic motion on a strange attractor in a dissipative system, the equilibrium invariant distribution is not known *a priori* and must be found for each attractor of interest. A method for obtaining this distribution has been developed for maps of the form (53) [42-43], in the parameter regime (ε, δ) for which a strange attractor exists. The basic assumption is that the equilibrium invariant distribution, averaged over the unperturbed angle variable, can be determined from a Fokker-Planck equation in the action alone. Successively better approximations to the invariant distribution are then found by repeated iteration of the angle-averaged distribution over the map. Typically only a few iterations are required.

The phase-averaged invariant distribution $f(y)$ is determined from the steady state $(\partial/\partial n \equiv 0)$ Fokker-Planck equation (54). This equilibrium solution is a good initial guess for the invariant distribution. To find better approximations for the equilibrium invariant distribution $f(x, y)$, we note that

almost every initial distribution $f^{(0)}(x, y)$ within the basin B converges under repeated iteration of the map to f. We choose an $f^{(0)}$ for a fast rate of convergence to the equilibrium distribution:

$$f^{(0)}(x, y) = f(y). \tag{75}$$

To find successively higher order approximations, we iterate (75) successively by the map. Letting $z' = (x', y')$ be the pre-image of $z = (x, y)$, and $z_{n+1} = T z_n$, where T is the map (53), then the i and $i + 1$ approximations are related by

$$f^{(i+1)}(x, y) dx dy = f^{(i)}(x', y') dx' dy',$$

which yields

$$f^{(i+1)}(z) = Jf^{(i)}(z'(z)), \tag{76}$$

where $J(T^{-1}z) = |\partial(x', y')/\partial(x, y)|$ is the Jacobian of the inverse map $T^{-1}z = z'(z)$. The first order invariant distribution is then

$$f^{(1)}(z) = J(T^{-1}z)f^{(0)}(T^{-1}z). \tag{77}$$

By repeatedly applying (76) we obtain the nth order approximation

$$f^{(n)}(z) = f^{(0)}(T^{-n}z) \prod_{i=1}^{n} J(T^{-i}z). \tag{78}$$

Equations (75) and (78) have been verified for strange attractors in both the dissipative Fermi map (64) and the dissipative standard map [42,40]. As an example, for the Fermi map with $M = 100$, numerical computations suggest that a strange attractor exists for $\delta > 0.03$. A typical case is $\delta = 0.1$. Figure 16a shows a portion of the (u, ψ) surface of section in the range $4.4 \leq u \leq 4.8$. The leaved structure of the attractor is quite evident. There are finer structures within the leaves. Here the region has been divided into 100 intervals along u and 100 intervals along ψ, forming 10,000 cells. The map is iterated 3×10^6 times for a single initial condition, and the number inside each cell (not readily seen) is a logarithmic measure of the number of occupations. If the number of occupations per cell is summed over the phases ψ at a fixed u, the phase-averaged invariant distribution $f(u)$ is obtained numerically.

To determine f analytically, the phase-averaged Fokker-Planck equation (54) is used. In the steady state, with no net flux, this equation becomes

$$-Bf + \frac{1}{2} D \frac{df}{du} = 0. \tag{79}$$

With $\delta \geq .01$, the distribution is mainly confined to $u < u_s$ such that the quasilinear value $D = \frac{1}{2}$ is a good approximation. Using $B = -\delta u$ from (55), (79) is integrated to obtain

$$f(u) = \left[\frac{8\delta}{\pi} \right]^{1/2} \exp(-2\delta u^2). \tag{80}$$

In Fig. 17, this analytical expression (solid line) is compared with the numerical results for $\delta = 0.1$ and various values of M in the range 20-500. The numerical points all lie along the same straight line, independent of M, as predicted by (80).

To find the first order distribution, (77) is used with $J = (1 - \delta)^{-1}$ and, inverting the Fermi map, one obtains

$$f^{(1)}(\psi, u) = \frac{1}{1 - \delta} \left[\frac{8\delta}{\pi} \right]^{1/2} \times \exp\left\{ -\frac{2\delta}{(1 - \delta)^2} \left[u + \sin\left[\psi - \frac{2\pi M}{u} \right] \right]^2 \right\}. \tag{81}$$

To compare (81) with the numerically calculated invariant distribution $f(\psi, u)$, the expected occupation number is plotted in Fig. 16b using $f^{(1)}$, in the same expanded region of the surface of section as for the numerical calculation of f in Fig. 16a. The same number of total occupations (3×10^6) and the same logarithmic measure for the number of occupations in each of the 100×100 cells are used. The band structure seen in the magnified image of $f^{(1)}$ corresponds closely to the numerically determined bands seen in Fig. 16a. The higher order expressions $f^{(2)}$ and $f^{(3)}$ have also been determined [42] and are plotted in Figs. 16c and 16d. These show successively better agreement with the numerical calculation.

Phase averaged invariant distributions can also be found in the presence of sources and sinks, with the source strength determining the normalization of the distribution. For area-preserving maps, a solution to the Fokker-Planck equation with a source at u_1 and a sink at u_2 is

$$f(u) = \int_{u_1}^{u} \frac{A}{D(u)} \, du, \tag{82}$$

with A proportional to the source strength. For dissipative systems there is a competition between the dissipation and the flow which determines the invariant distribution. If we consider a source at low velocity, then for the dissipative Fermi mapping (64), the time independent Fokker-Planck equation, using D from (67), is

$$\frac{1}{4} \left[1 - \frac{u^2}{u_B^2} \right]^2 \frac{df}{du} + u \, \delta f = \Gamma. \tag{83}$$

Dividing by $\frac{1}{4}(1 - u^2/u_B^2)^2$ we see that the use of the integrating factor $\exp[\int 4u \, \delta/(1 - u^2/u_B^2)^2]$ immediately yields the solution

$$f = \exp\left[-\int \frac{4\delta u \, du}{(1 - u^2/u_B^2)^2} \right] \int \frac{du \, 4\Gamma}{(1 - u^2/u_B^2)^2} \exp\left[\int \frac{4\delta u \, du}{(1 - u^2/u_B^2)^2} \right]. \tag{84}$$

For flow dominated behavior (weak dissipation) we can approximate the solution as in (82), while for strong dissipation the solution approximates that given in (80). The transition region can be important in some physical problems, such as the stochastic acceleration of electrons in the r.f. sheaths of a capacitive discharge, in which the dissipation arises from interactions with the background gas [5].

REFERENCES

1. A. J. Lichtenberg and M. A. Lieberman, *Regular and Stochastic Motion,* (Springer, New York, 1983).

2. J. Ford and J. Waters, *J. Math. Phys.,* 4, 1297 (1963).

3. M. A. Lieberman and A. J. Lichtenberg, *Phys. Rev. A* 5, 1852 (1972).

4. F. Jaeger, A. J. Lichtenberg, and M. A. Lieberman, *Plasma Phys.,* 14, 1073 (1972); M. A. Lieberman and A. J. Lichtenberg, *Plasma Phys.,* 15, 125 (1973).

5. V. Godyak, *Sov. J. of Plasma Phys.,* 2, 78 (1976); C. G. Goedde, A. J. Lichtenberg, and M. A. Lieberman, *Bull. APS,* 30, 1392 (1985).

6. J. Randrup and W. J. Swiateki, *Ann. Phys.,* 125, 193 (1980).

7. B. V. Chirikov, *Phys. Rep.,* 52, 263 (1979).

8. L. D. Pustylnikov, *Trans. Moscow Math. Soc.,* 2, 1 (1978).

9. A. J. Lichtenberg, M. A. Lieberman, and R. Cohen, *Physica* 1D, 291 (1980)

10. A. J. Lichtenberg, M. A. Lieberman, J. E. Howard, and R. H. Cohen, *Phys. Fluids,* 29, 1061 (1986).

11. G. M. Zaslavskii and B. V. Chirikov, *Sov. Phys. Dokl.,* 9, 989 (1965).

12. A. J. Lichtenberg, *Physica* 14D, 387 (1985).

13. J. M. Green, R. J. MacKay, F. Vivaldi, and M. J. Feigenbaum, *Physica* 3D, 468 (1981).

14. R. S. MacKay, J. D. Meiss, and I. C. Percival, *Physica* 13D, 55 (1984).

15. J. D. Meiss and E. Ott, *Phys. Rev. Lett.,* 55, 2741 (1985); *Physica* 20D, 387 (1986).

16. C. F. F. Karney, *Physica* 8D, 369 (1983).

17. A. J. Lichtenberg, M. A. Lieberman, and N. W. Murray, *Physica* 28D, 371 (1987).

18. M. C. Wang and G. E. Uhlenbeck, *Rev. Mod. Phys.,* 17, 523 (1945).

19. L. D. Landau, *Zh. Eksper. Theor. Fiz.,* 7, 203 (1937); see also ref. 1, Sec. 5.4a.

20. A. B. Rechester and R. B. White, *Phys. Rev. Lett.*, 44, 1586 (1980); A. B. Rechester, M. N. Rosenbluth, and R. B. White, *Phys. Rev. A*, 23, 2664 (1981).

21. H. D. I. Abarbanel, *Physica* 4D, 89 (1981); see also ref. 1, Sec. 5.4d.

22. J. R. Cary, J. D. Meiss, and A. Bhattacharee, *Phys. Rev. A*, 23, 2744 (1981).

23. J. D. Meiss, J. R. Cary, C. Grebogi, J. D. Crawford, A. N. Kaufman, and H. D. I. Abarbanel, *Physica* 6D, 375 (1983).

24. N. W. Murray, M. A. Lieberman, and A. J. Lichtenberg, *Phys. Rev. A*, 32, 2413 (1985).

25. B. V. Chirikov and D. L. Shepelyansky, *Physica* 13D, 395 (1984); see also Preprint 86-174, Inst. of Nucl. Phys., Novosibirsk (1986).

26. V. I. Arnold and A. Avez, *Ergodic Problems of Classical Mechanics*, Benjamin, NY (1968).

27. A.V. Timofeev, *Sov. Phys.-JETP* 48, 656 (1978).

28. B.V. Chirikov, F.M. Izrailev, and D.L. Shepelyansky, *Sov. Sci. Rev.* C2, 209 (1981).

29. J.L. Tennyson, J.R. Cary, and D.F. Escande, *Phys. Rev. Lett.* 56, 2117 (1986).

30. J.R. Cary, D.F. Escande, and J.L. Tennyson, *Phys. Rev. A* 34, 4256 (1986).

31. B. V. Chirikov and F. M. Izraelev, Colloques Internationaux du C.N.R.S. (Toulouse, 1973); No. 229, p. 409, Paris (1976).

32. B. V. Chirikov and F. M. Izraelev, *Physica* 2D, 30 (1984).

33. C. Grebogi, E. Ott, and J. A. Yorke, *Phys. Rev. Lett.*, 57, 1284 (1986).

34. J. B. McLaughlin, *Phys. Lett.*, 72A, 271 (1978).

35. K. Y. Tsang and M. A. Lieberman, *Physica* 21D, 401 (1986).

36. F. M. Izraelev, B. Timmermann, and W. Timmermann, "Transient Chaos in a Generalized Henon Map on a Torus," Preprint 87-1, Inst. of Nucl. Phys., Novosibirsk, USSR (1987).

37. M. Henon, *Comm. Math. Phys.*, 50, 69 (1976).

38. H. C. Osbourne, *IEEE Trans. Commun.*, COM-28, 1343 (1980); 1355 (1980).

39. G. M. Bernstein, M. A. Lieberman, and A. J. Lichtenberg, "Nonlinear Dynamics of a Digital Phase Locked Loop," Memo UCB/ERL M87/59, College of Engineering, University of California, Berkeley (1987); submitted to *IEEE Trans. Commun.*

40. B. V. Chirikov, *Phys. Rep.*, 52, 263, Table 5.3 (1979).

41. N. W. Murray, M. A. Lieberman, and A. J. Lichtenberg, *Phys. Rev.*, A32, 2413 (1985).

42. K. Y. Tsang and M. A. Lieberman, *Physica* 11D, 147 (1984).

43. K. Y. Tsang and M. A. Lieberman, *Phys. Lett.*, 103A, 175 (1984).

44. M. A. Lieberman and K. Y. Tsang, *Phys. Rev. Lett.*, 55, 908 (1985).

45. J. A. Yorke and E. D. Yorke, *J. Stat. Phys.*, 21, 263 (1979).

46. C. Grebogi, E. Ott, and J. A. Yorke, *Physica* 7D, 181 (1983).

47. M. Widom, D. Bensimon, L. P. Kadanoff, and S. J. Shenkar, *J. Stat. Phys.*, 32, 443 (1983).

48. L. P. Kadanoff and C. Tang, *Proc. Natl. Acad. Sci.*, 81, 1276 (1984).

49. H. Kantz and P. Grassberger, *Physica* 17D, 75 (1985).

50. P. Szépfalusy and T. Tél, *Phys. Rev.* A34, 2520 (1986).

51. J. D. Farmer, *Physica* 4D, 336 (1982).
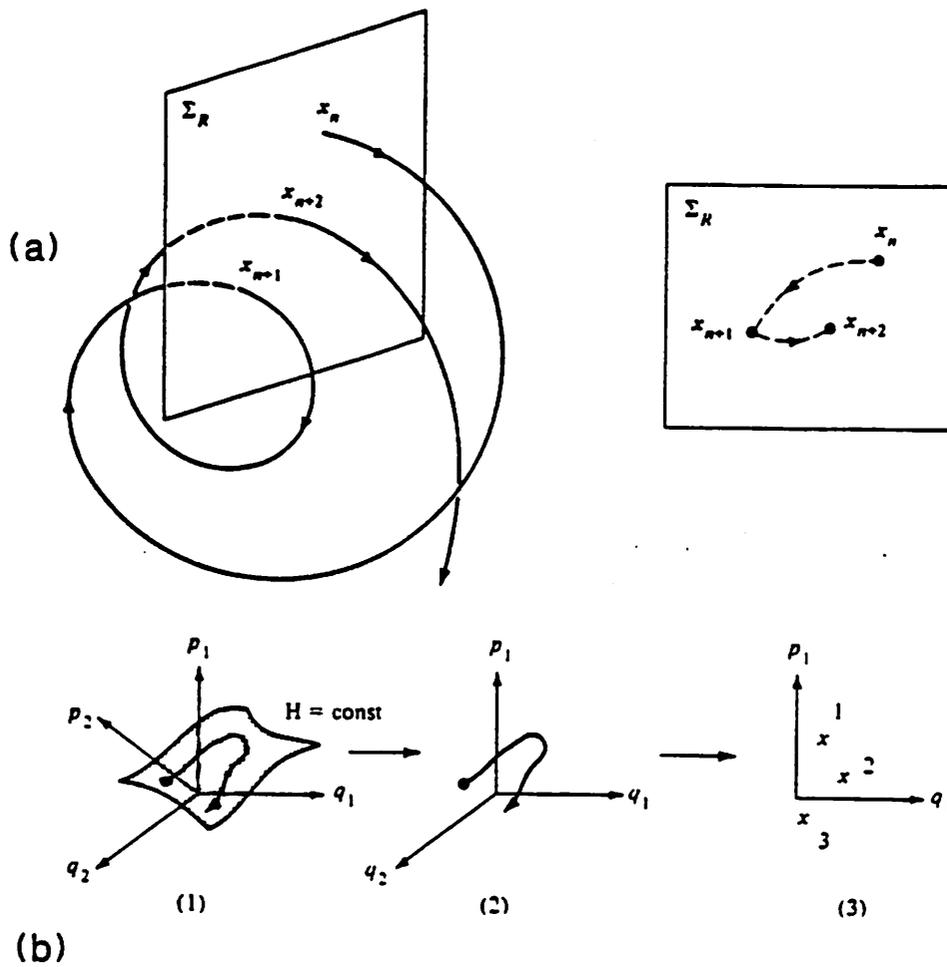
Figure 1.   Motion in phase space and definition of the Poincare surface of section. (a) Intersections of a trajectory with the surface of section. (b) Two degrees of freedom showing: (1) four-dimensional phase space with the trajectory on a three-dimensional energy surface; (2) projection of the trajectory onto the (p_1, q_1, q_2) volume; and (3) successive intersections of the trajectory with the two-dimensional surface of section $q_2 = $ const [ref. 1].
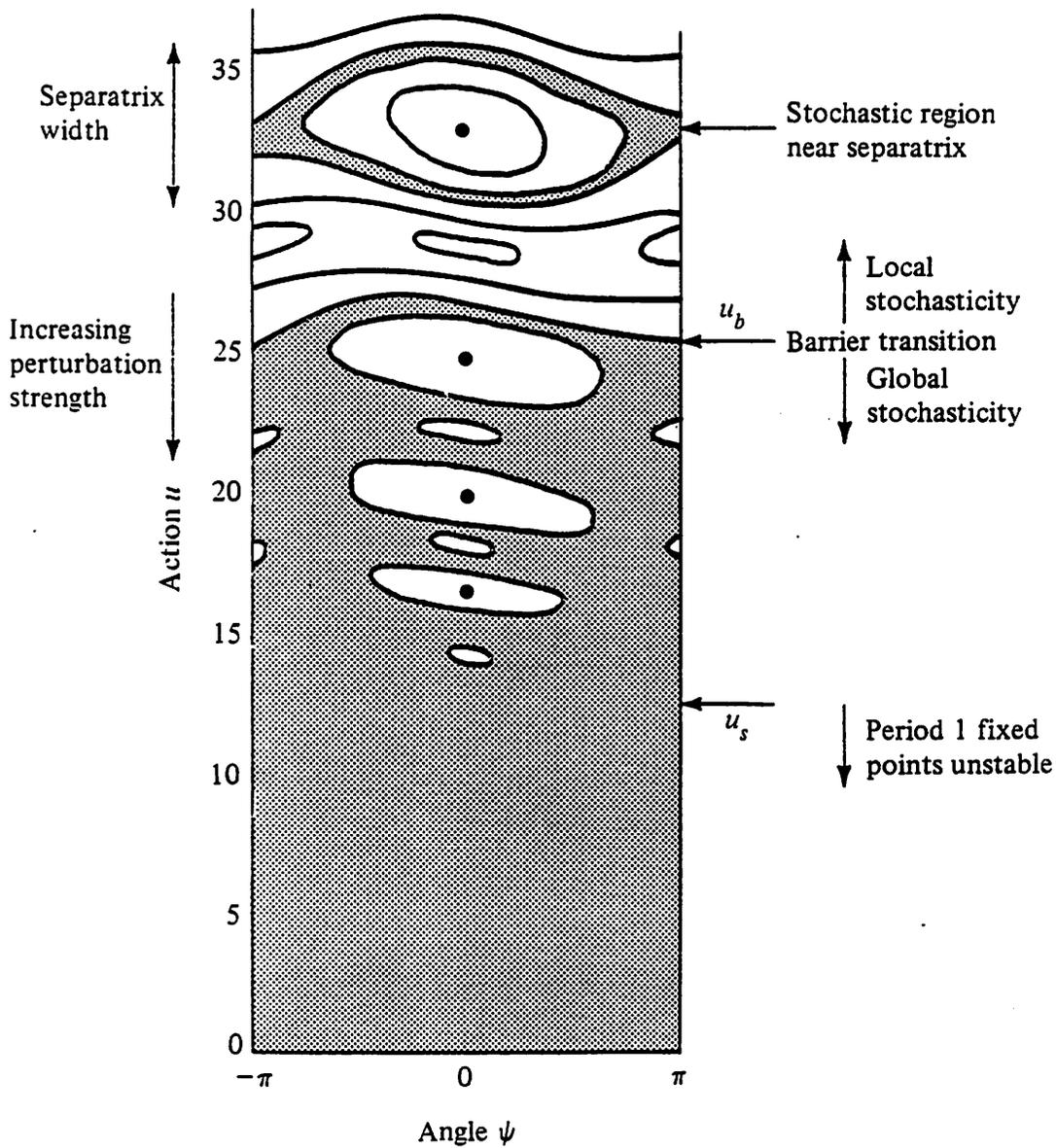
Figure 2. An illustration of the transition from local to global stochasticity as the perturbation strength is increased [ref. 1].
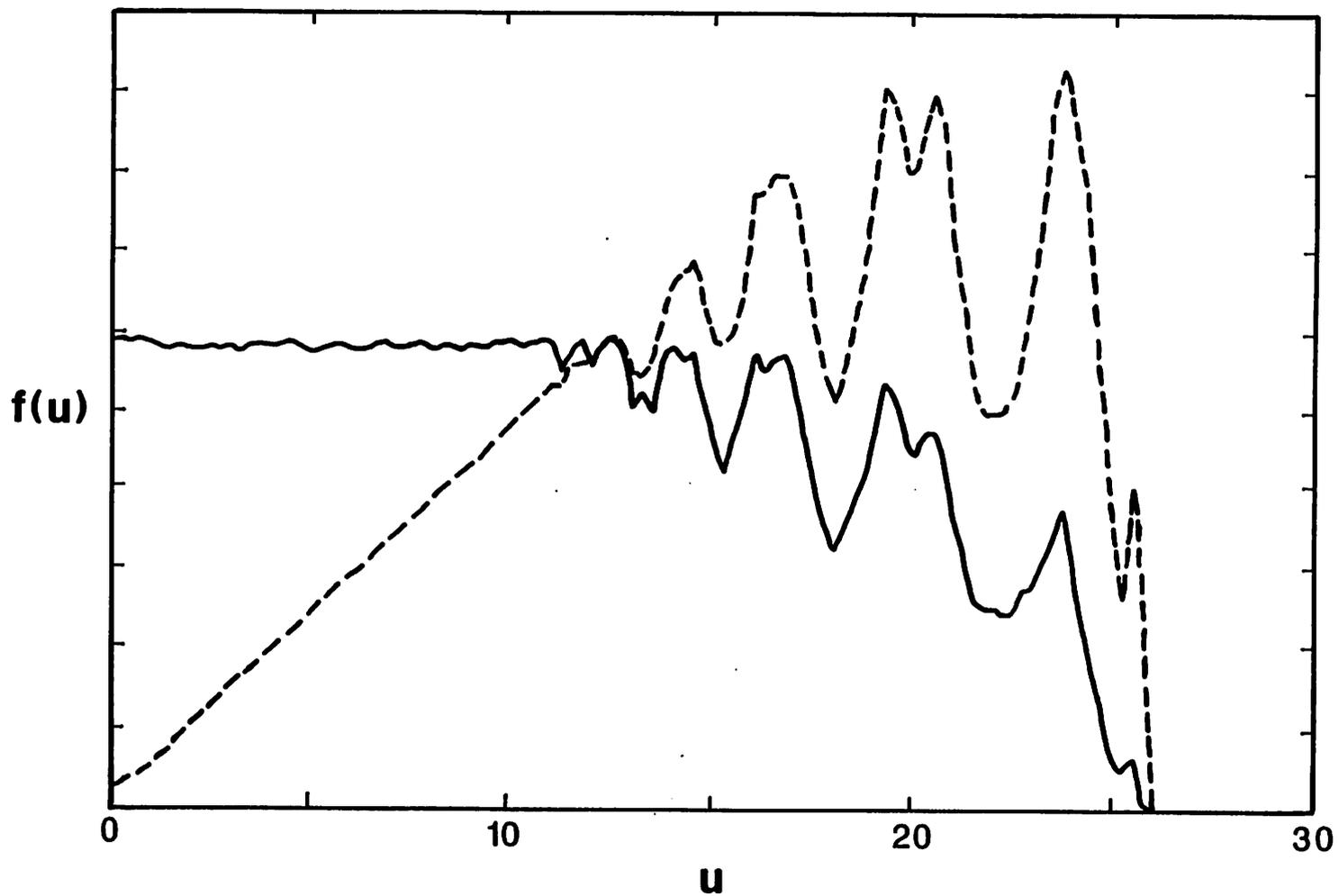
Figure 3. Comparison of velocity distribution $f(u)$ for the approximate Fermi map (7) [solid line]

and the moving wall Fermi map (22) [dashed line].

(a)

(b)

(c)
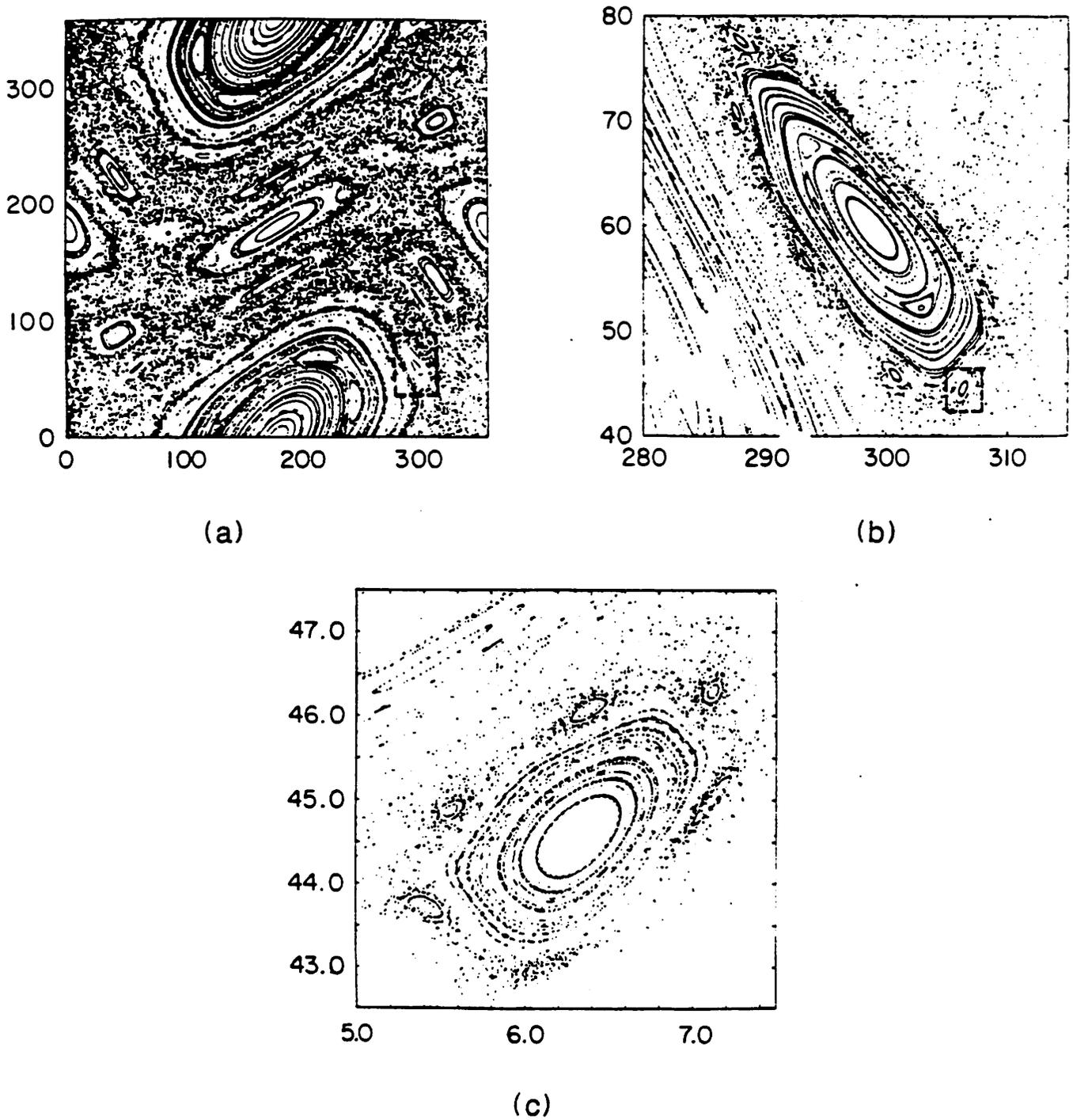
Figure 4.   The standard map; ordinate I, abscissa θ (in degrees); (a), (b), (c). $K = 1.19$; 150 random

initial conditions for each graph; number of iterations increasing downward as $N = 500$,

5000, and 10,000. In (b) the boxed region in (a) is magnified; in (c), the boxed region in

(b) is further magnified [ref. 12].
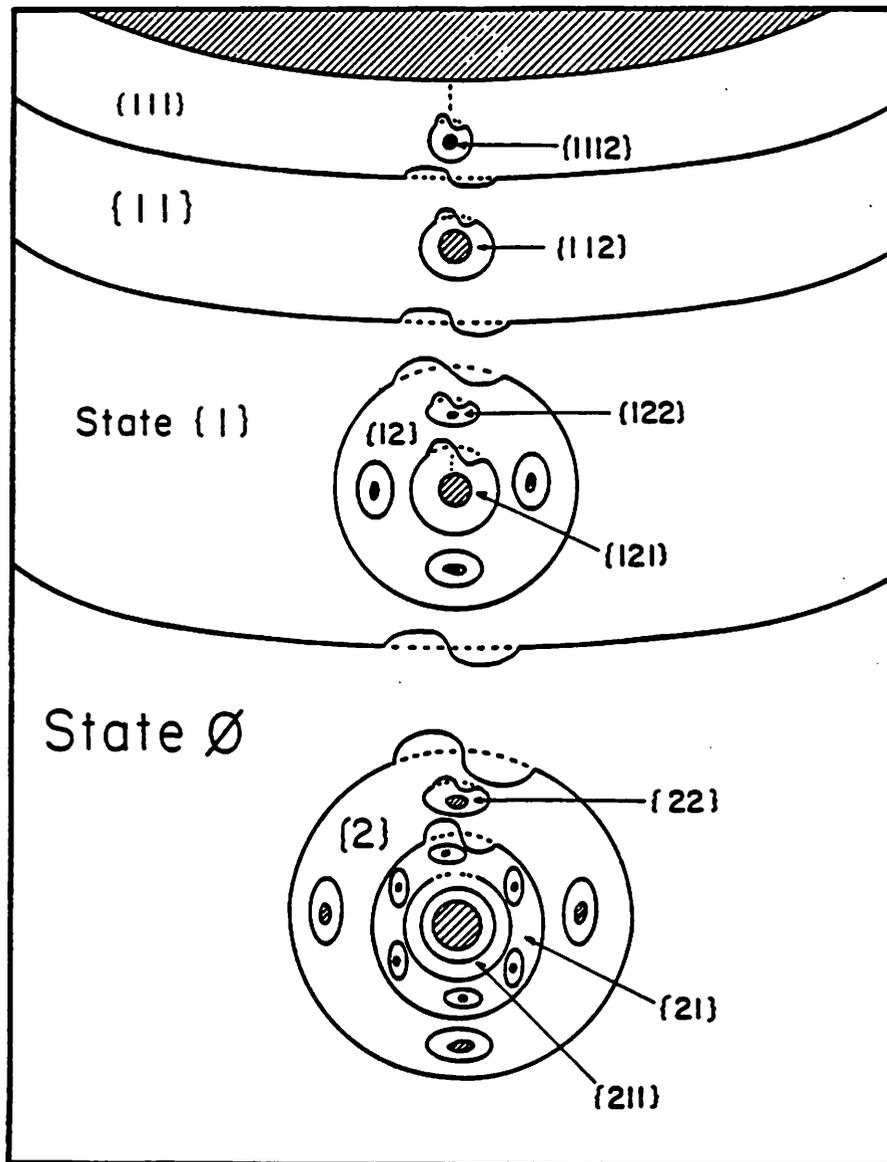
Figure 5. Schematic illustration of connected chaotic regions of an area-preserving map bounded by low-flux cantori (states). Inaccessible regions surrounded by an outermost KAM island surface are shown crosshatched [ref. 15].
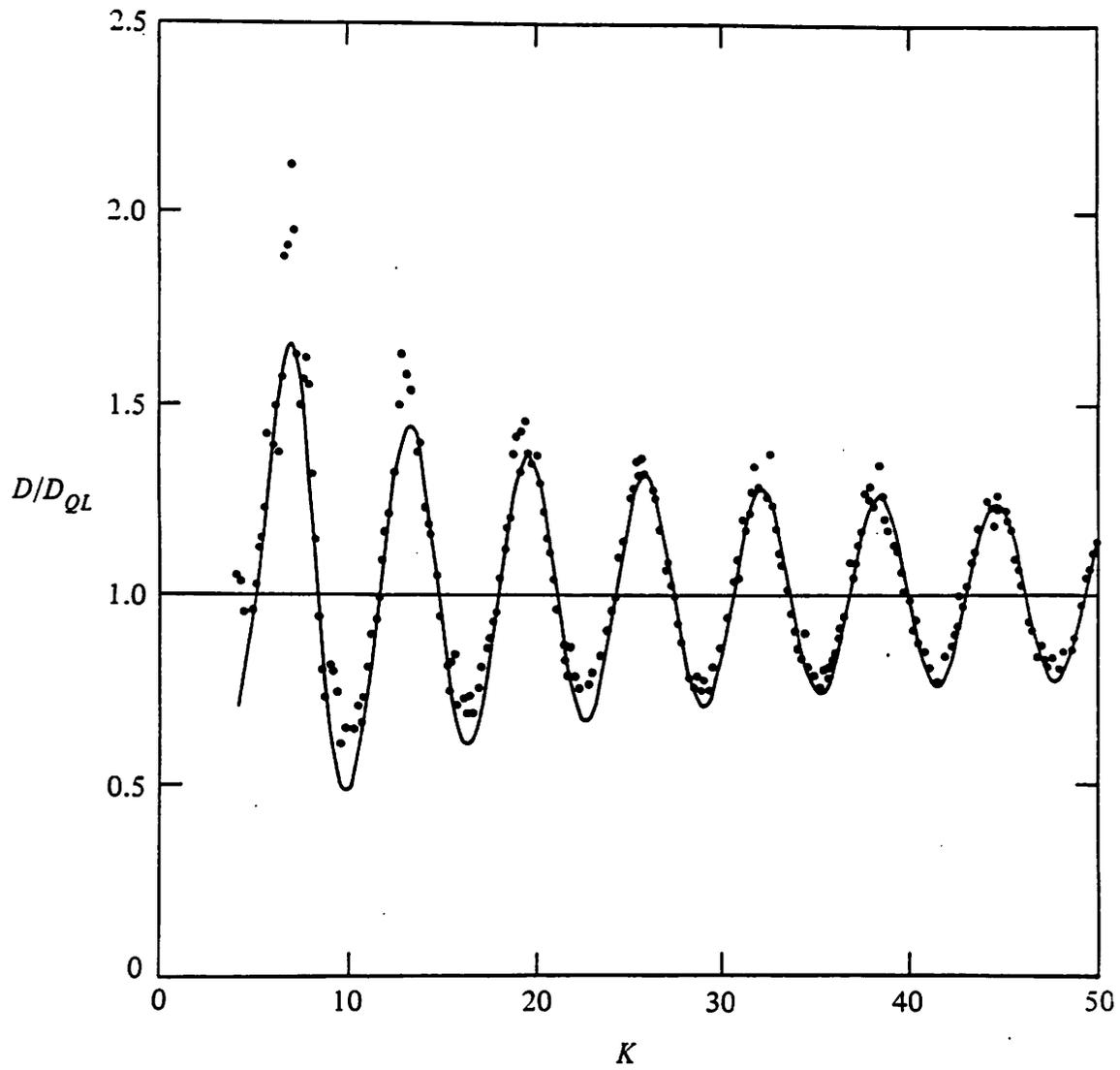
Figure 6. Plot of D/D_{QL} versus stochasticity parameter K. The dots are the numerically computed values and the solid line is the theoretical result in the large K limit [ref. 20].
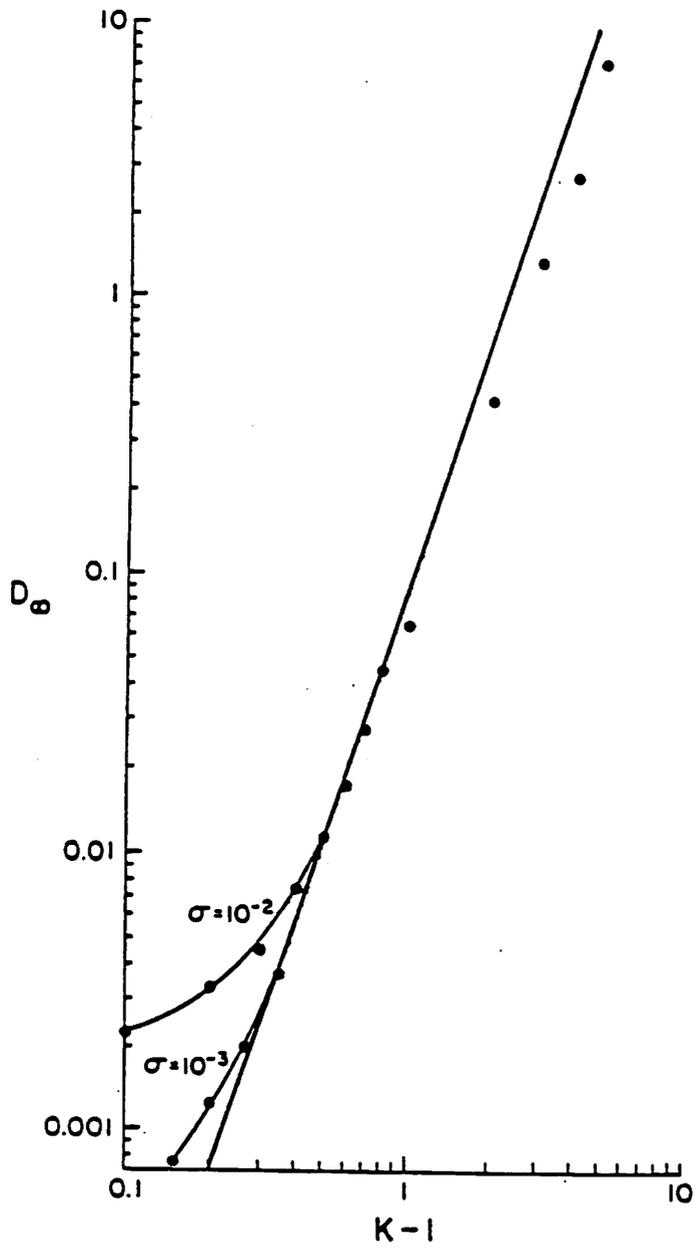
Figure 7. $D_\infty(K)$ vs. K, from A. B. Rechester and R. B. White, private communication; see ref. 24.
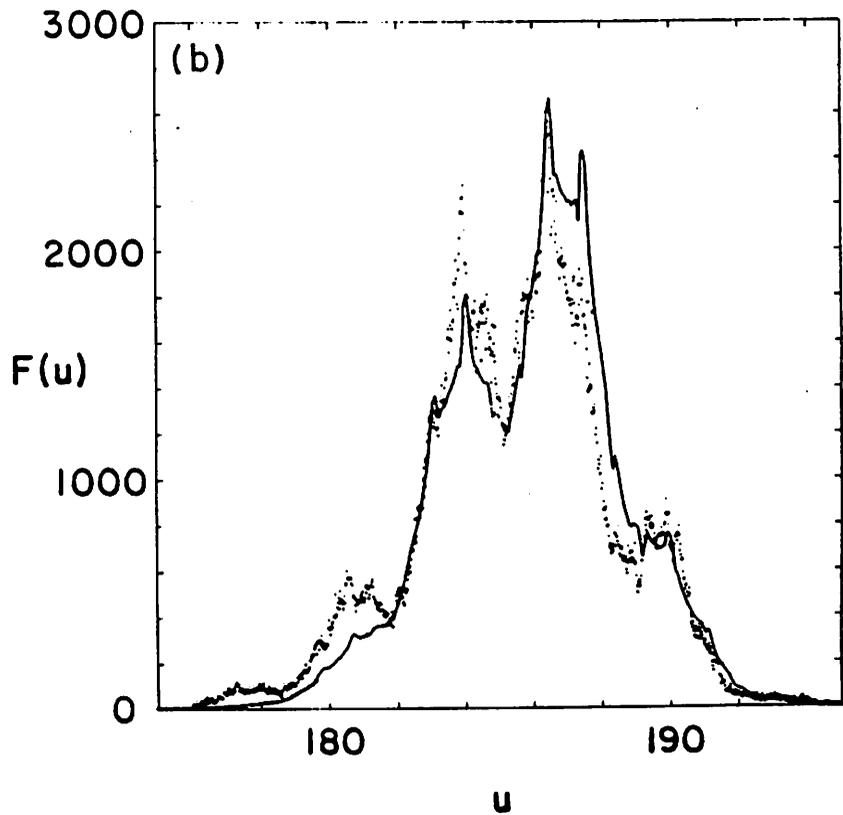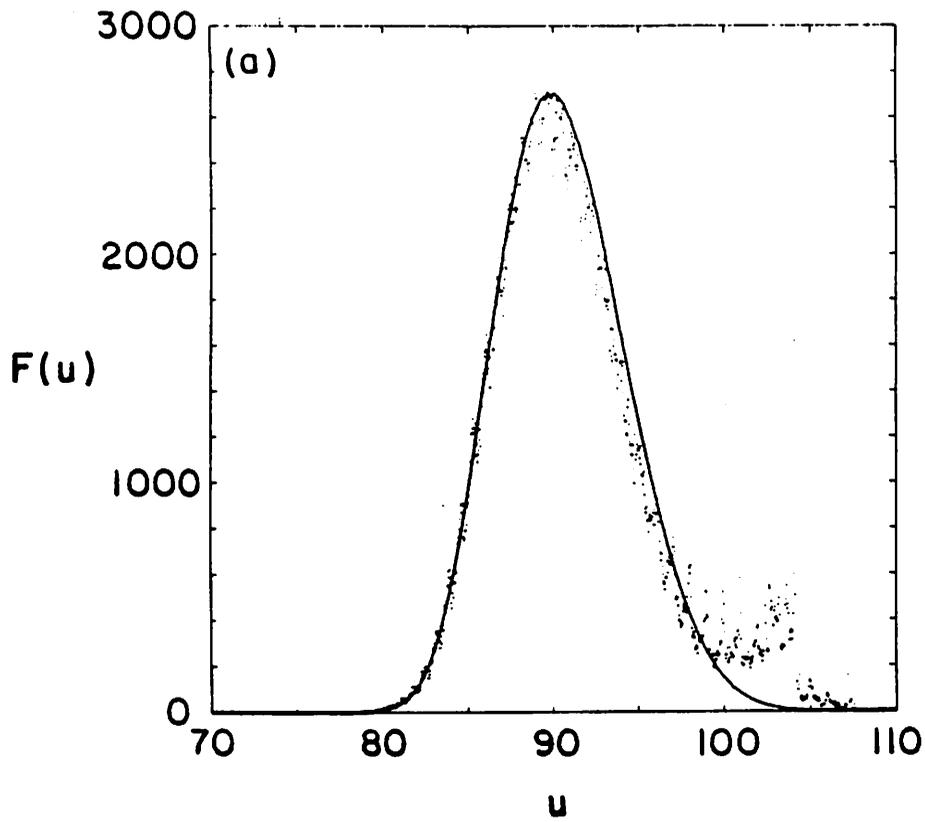
Figure 8.   (a) The distribution function obtained by iterating 6400 initial conditions with $u_0 = 90$ and

random phases.   The dots indicate the number of particles within $\Delta u = .025$ at a given

action. The solid line is the prediction of the Fokker-Planck equation; (b) the same as (a),

with $u_0 = 186$ [ref. 24].
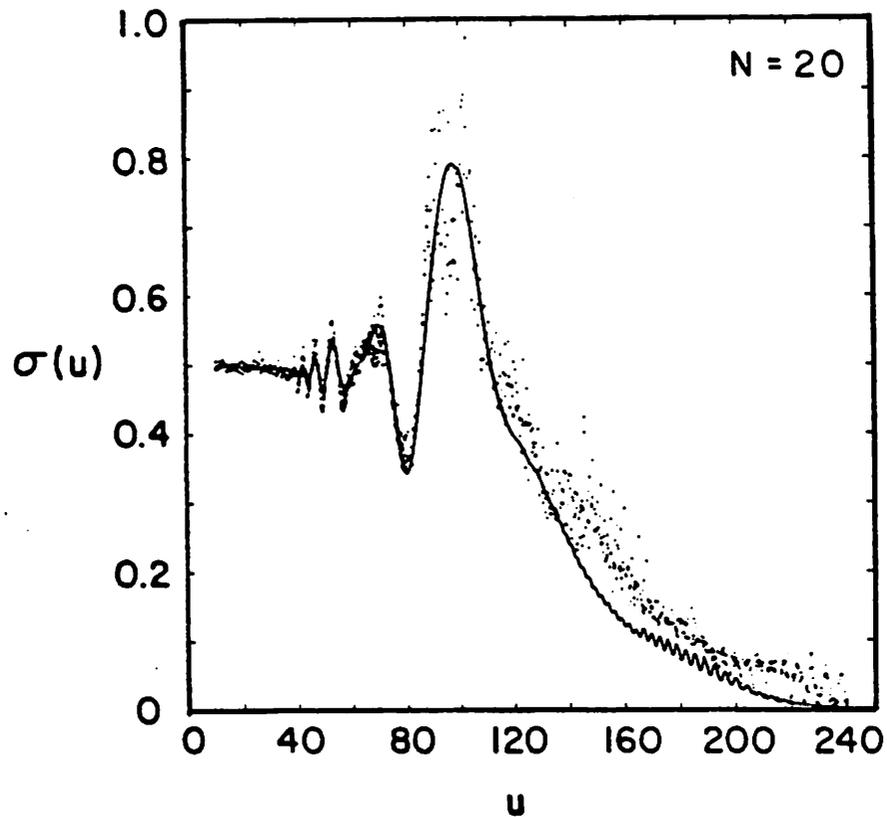
Figure 9.   The variance plotted as a function of initial action. Each dot corresponds to a measurement of the diffusion obtained by iterating the Fermi map. The solid line is the theoretical variance obtained by integrating Fokker-Planck equation; (a) after 20 iterations; (b) after 40 iterations [ref. 24].
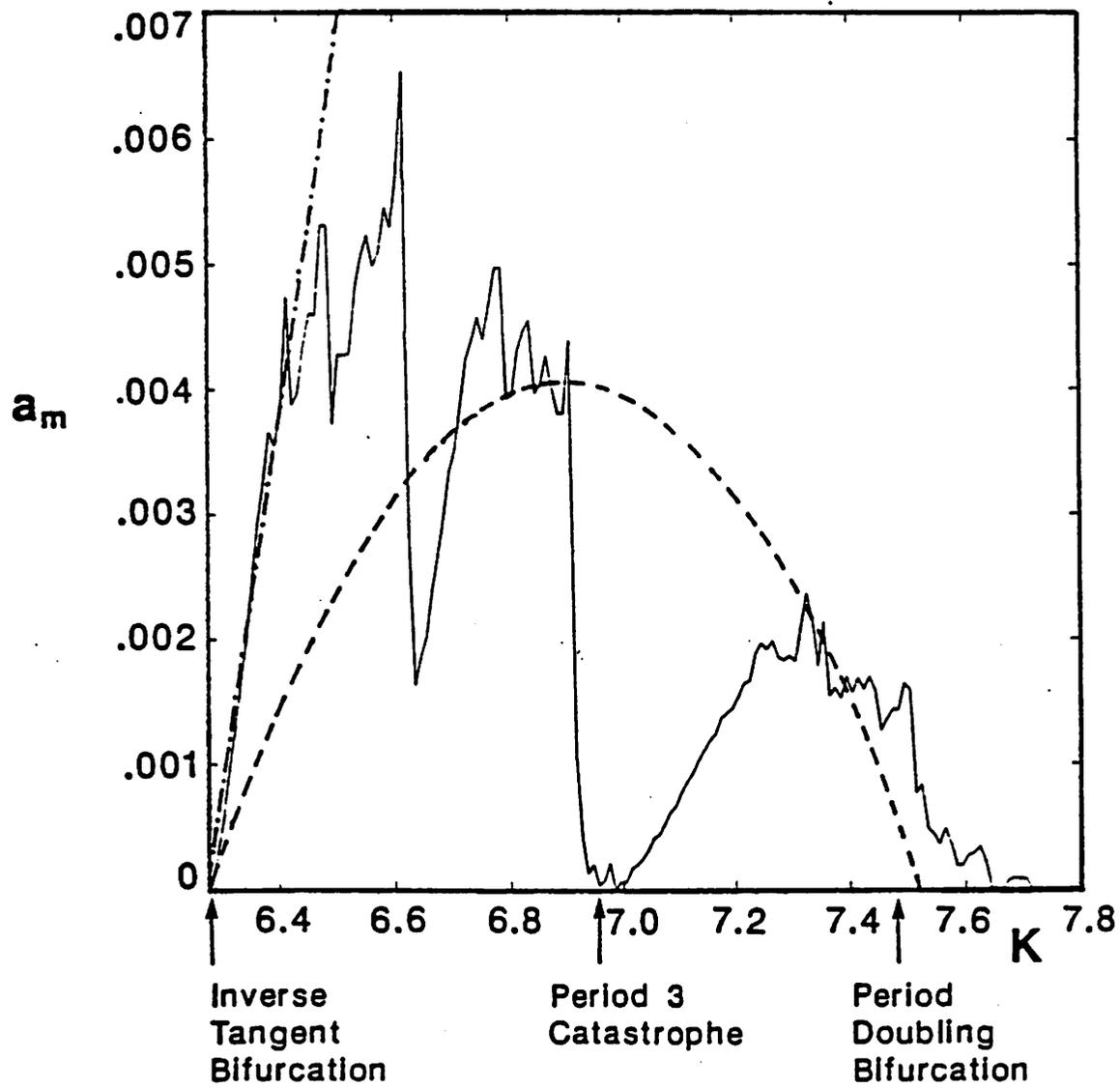
Figure 10.   Stable area of the first accelerator mode of the standard map as a function of K, normalized to the map area $(2\pi)^2$ [ref. 17].
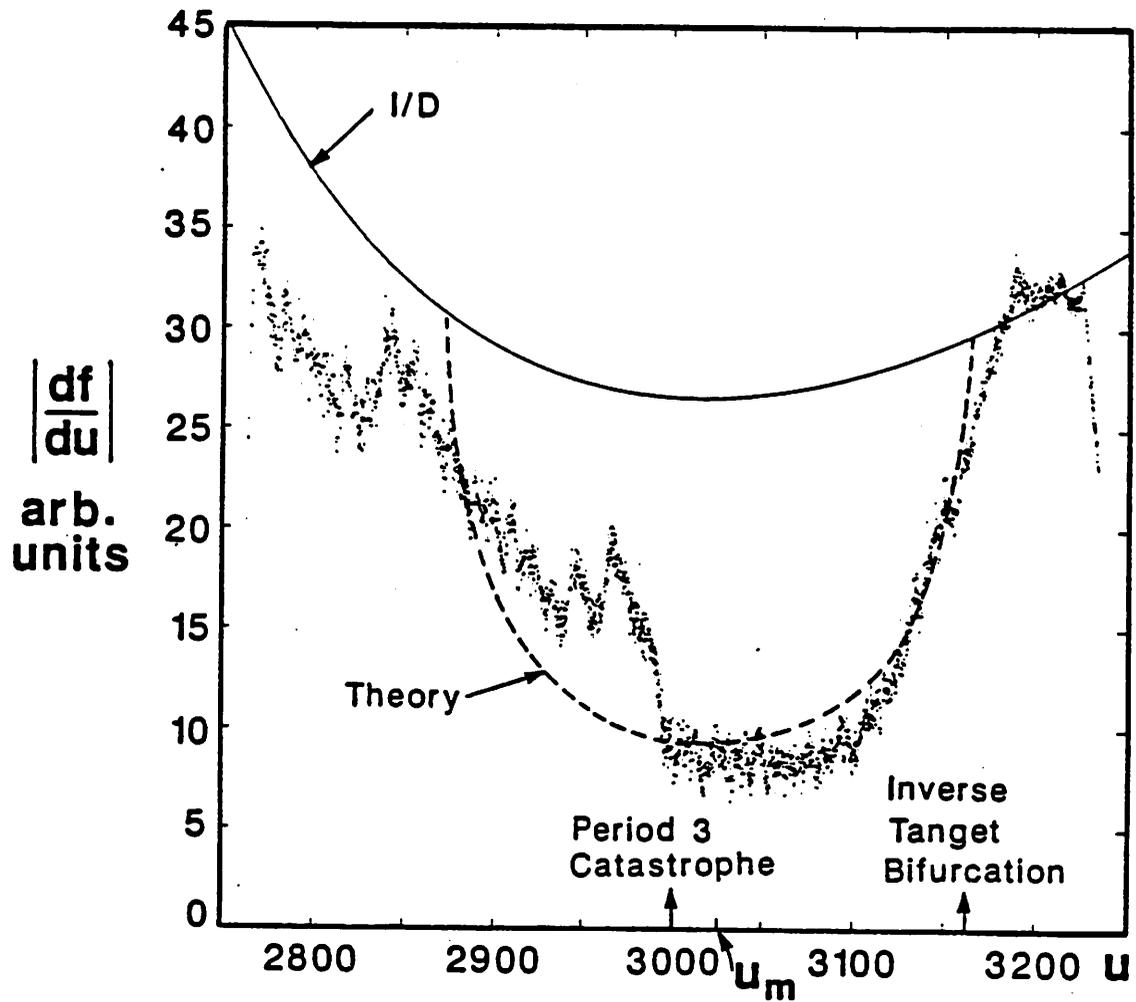
Figure 11.   Comparison of theoretical and numerical relative values of $|df/du|$. The theoretical value

is shown as a dashed curve within the mode and a solid curve ($\propto$ $1/D$) outside of the

mode ($M = 10^7$) [ref. 17].
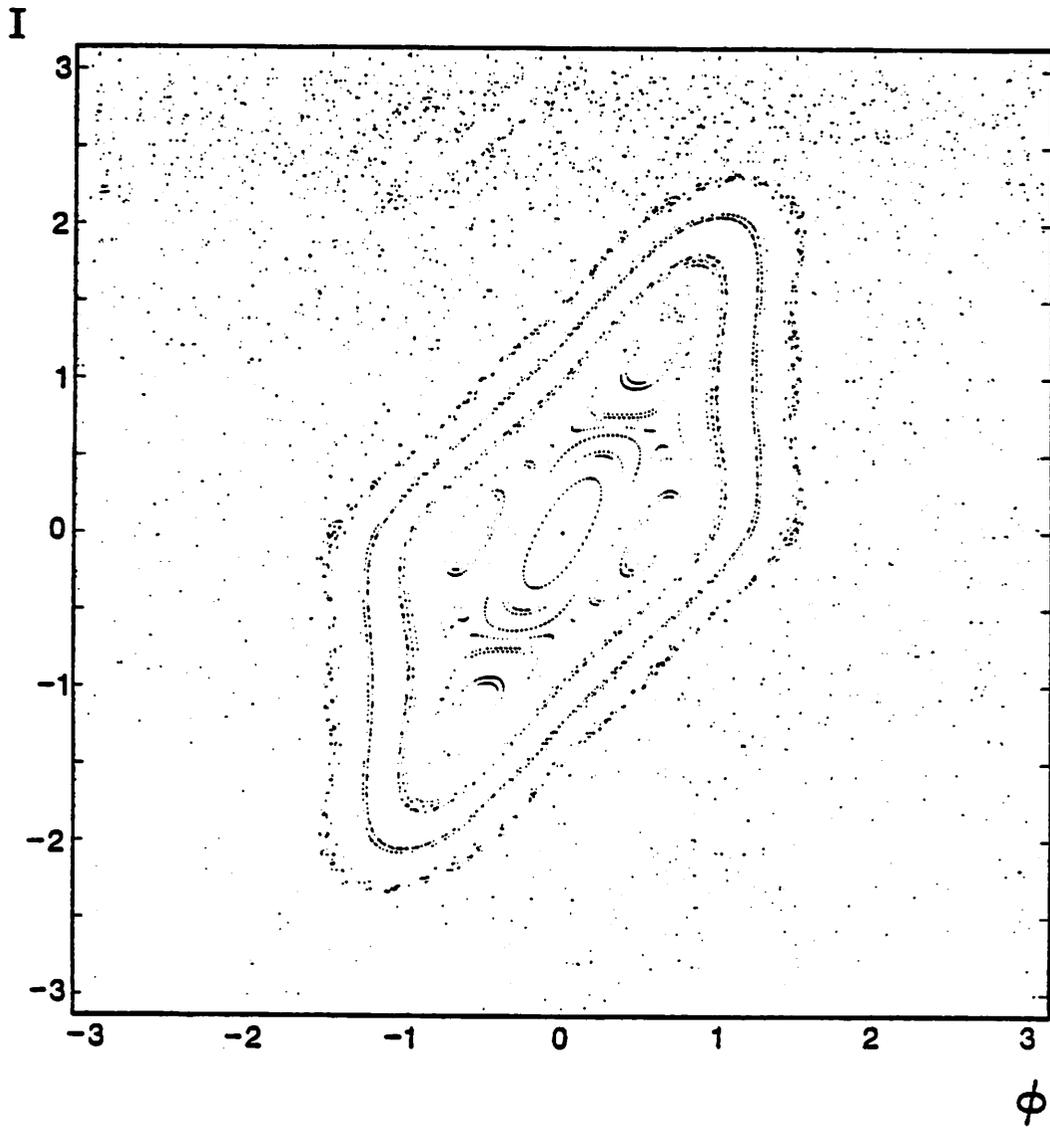
Figure 12. I versus ϕ for the standard map at $K = 2.13$ [ref. 36].
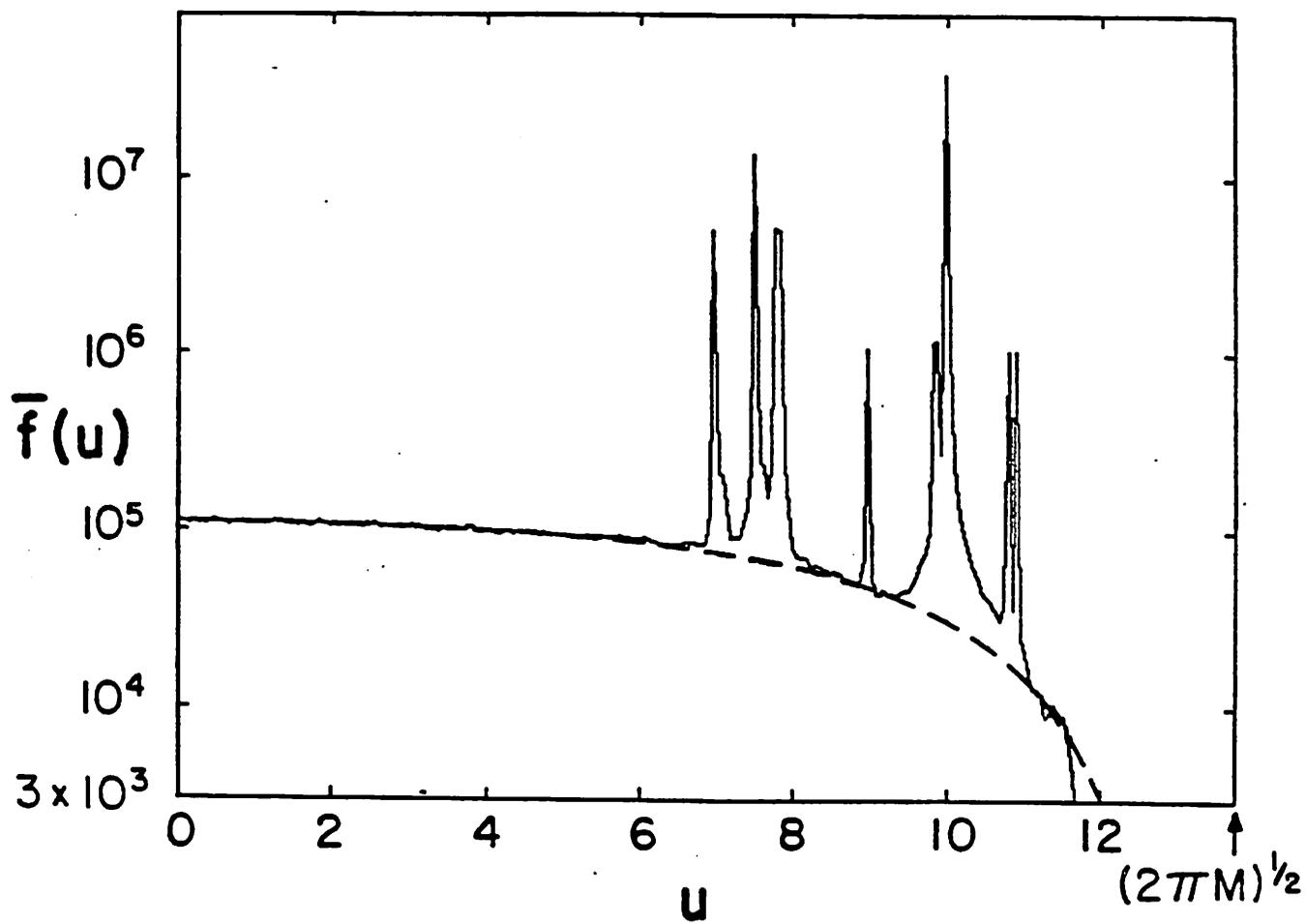
Figure 13.   Cumulative, phase-averaged distribution $\overline{f}$ vs. u, for $M = 30$, $\delta = 0.003$, and $N = 5 \times 10^4$
iterations. The solid curve shows the numerical result; the dashed curve shows the quasis-
tatic theory [ref. 41].
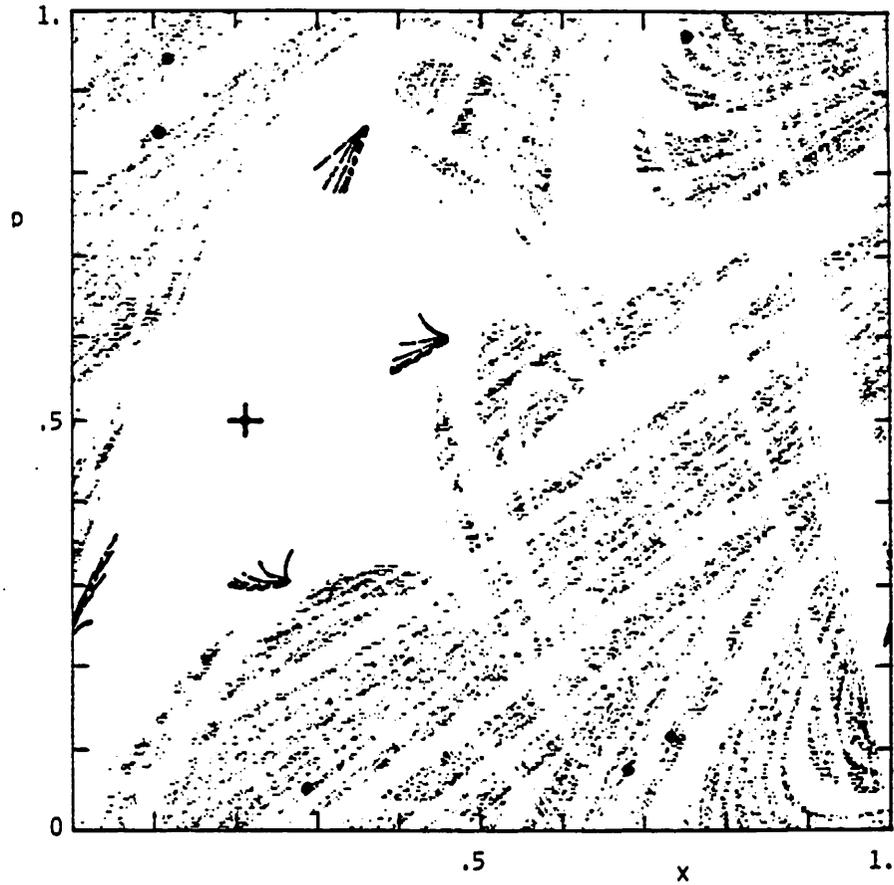
Figure 14. Attractors and repellers of the map defined by (52) with $\delta = 0.1$ and $K = 3.5$. The cross at $(x, p) = (0.2113, 0.5)$ is the main attractor. A second attractor with a very small basin is made up by the six heavy dots. The four fans around the main attractor represent the semi-attractor which governs the long-time transients. The remaining points form a repeller with shorter life time [ref. 46].
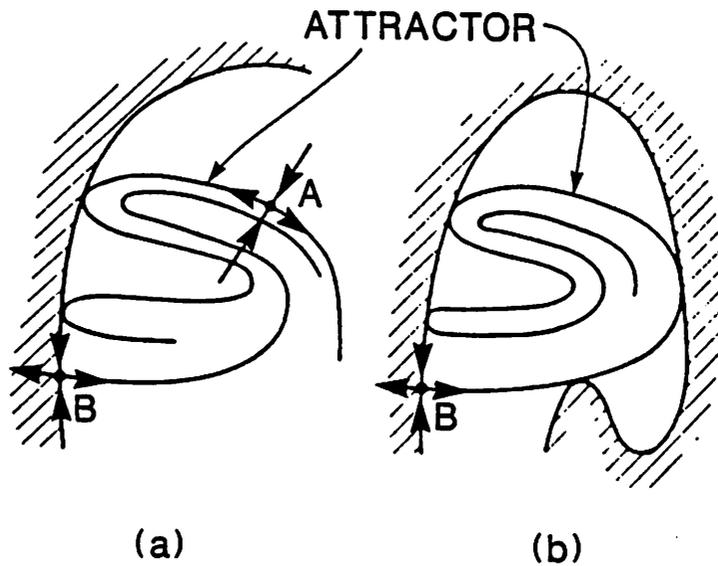
Figure 15.   (a) Schematic illustration of heteroclinic tangencies of the stable manifold of the unstable periodic orbit B and the unstable manifold of the unstable periodic orbit A. (For simplicity we take the periods of A and B to be 1.) Crosshatching denotes the basin of another attractor.   (b) Schematic illustration of homoclinic tangencies of the stable and unstable manifolds of the unstable periodic orbit B [ref. 30].
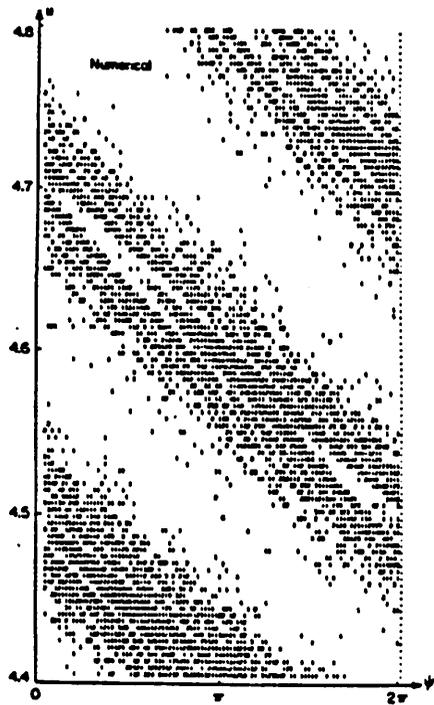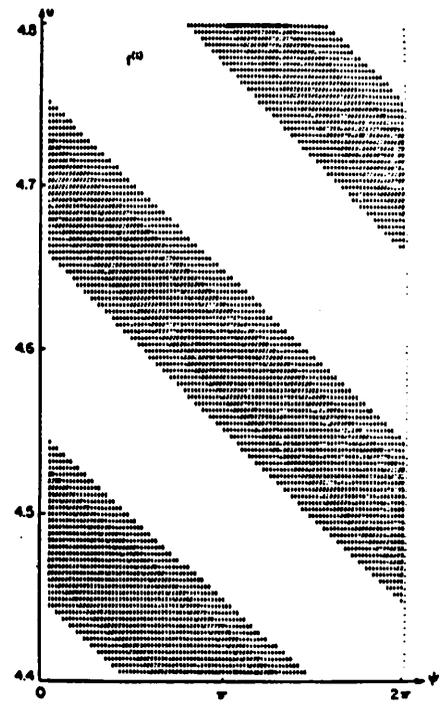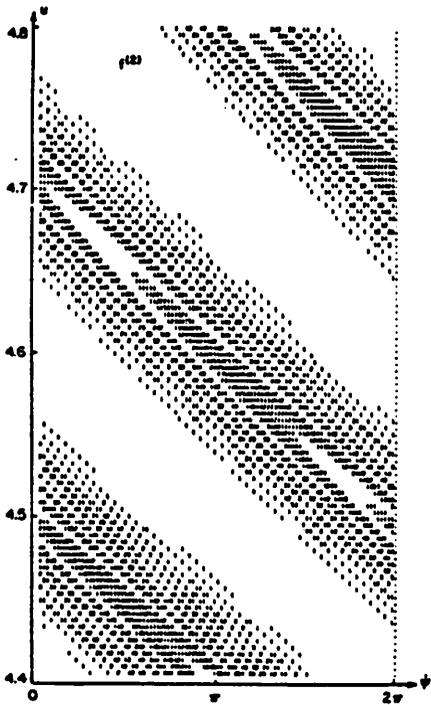
Figure 16. A portion of the surface of section $u-\psi$ for the Fermi map with $M = 100$ and $\delta = 0.1$. (a) one particle with 3,000,000 collisions, of which 9382 occupations appear in the range $4.4 \leq u < 4.8$. (b) first order analytical result $f^{(1)}(\psi, u)$; (c) second order result $f^{(2)}(\psi, u)$; (d) third order result $f^{(3)}(\psi, u)$; the functions are plotted by computer with the scales and effective number of iterations the same as for the numerical result (a) [ref. 39].
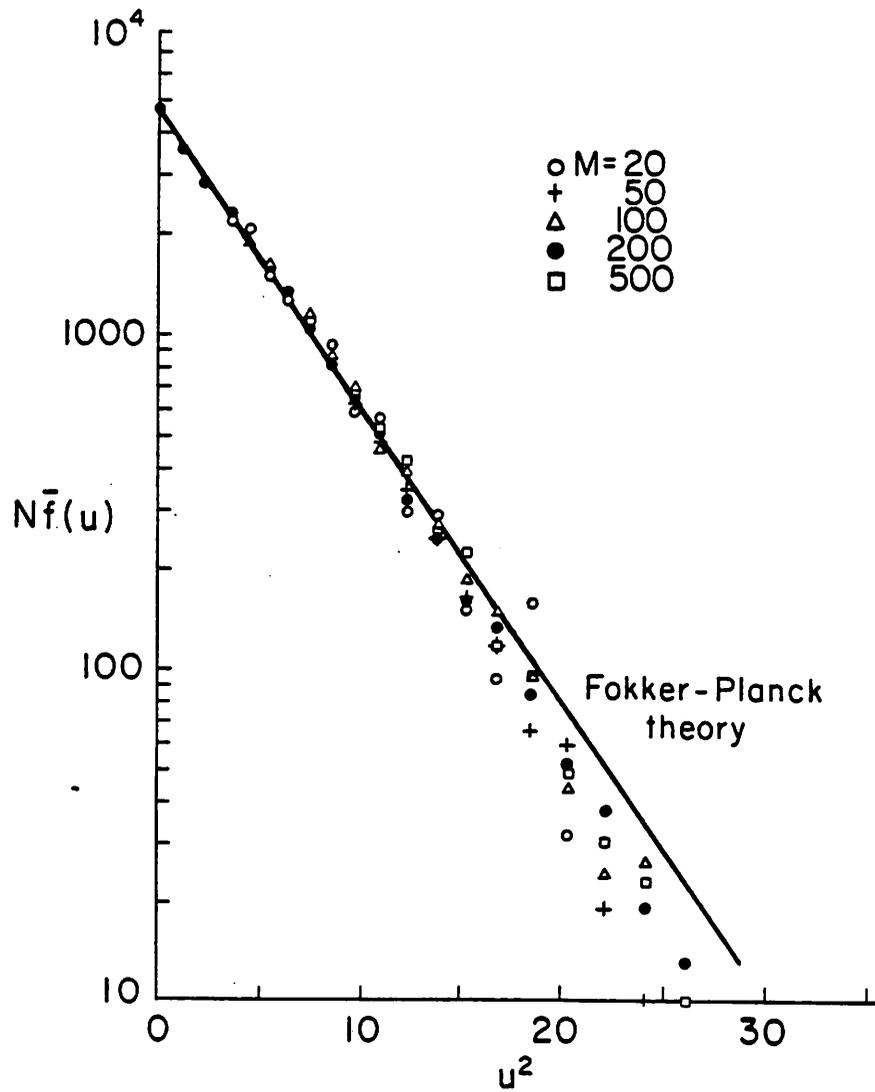
Figure 17. Comparison of the numerically calculated phase-averaged invariant distribution with the Fokker-Planck solution $f(u)$ for $\delta = 0.1$ and various values of M for the Fermi map [ref. 39].